UiT
THE ARCTIC UNIVERSITY OF NORWAY

Faculty of Science and Technology

Department of Physics and Technology

Investigation of Sea Ice Using Multiple Synthetic Aperture Radar Acquisitions

—

Temesgen Gebrie Yitayew

A dissertation for the degree of Philosophiae Doctor – November 2017

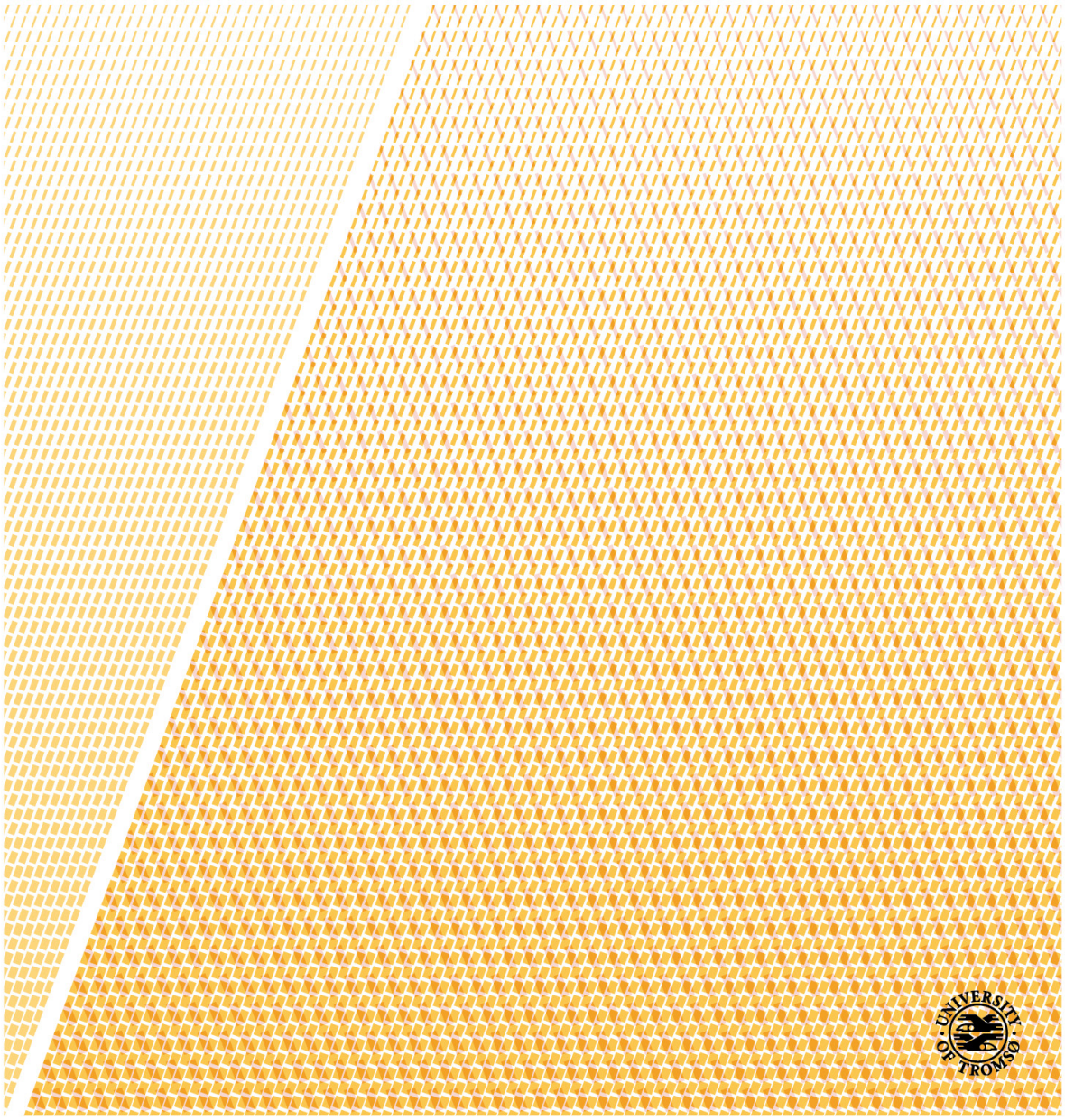

Abstract

Synthetic aperture radar (SAR) is a coherent imaging technique which operates at microwave frequencies and is capable of producing high resolution two dimensional images of an observed medium. High resolution capability is achieved by synthesising a long virtual aperture through the motion of a platform and using advanced signal processing techniques. Radar waves have a unique capability of penetrating deep into semi-transparent media such as snow, sea ice, glacier ice and forest, and interacting with their internal volumetric structure. However, the conventional SAR imaging technique, which is operated along a horizontal aperture, is not capable of separating scattering contributions in the vertical direction, and all contributions within the volume are projected onto a two-dimensional azimuth-slant range plane during the imaging process. Across-track interferometry exploits the phase difference between two or more SAR images to retrieve the topography of the observed scene, whereas synthetic aperture radar tomography synthesizes an additional virtual aperture in the elevation direction to directly image the full three-dimensional response of volumetric media. Most common application areas of these two techniques include forest, urban area, and natural terrain imaging. Their application for sea ice has however been limited by the dynamic nature of the ice and the challenges of collecting the corresponding datasets. This thesis investigates imaging in the vertical direction of different types of ice using the techniques of SAR tomography and across-track interferometry.

The work in this thesis consists of two parts and organized in three papers. The first part presents experimental results involving tomographic imaging of fjord and lake ice, using a ground-based SAR system operated at multiple frequencies and polarizations. The results from this first part are published in two journal papers, Papers I and II. The experiments were conducted at two test sites, namely Kattfjord and Prestvannet lake, both in the Tromsø area, in the northern part of Norway. In both cases, the test sites contain snow covered seasonal ice with a thickness of a few tens of centimeters. The distributions of the radar reflectivity of the investigated snow and ice layers are presented in the form of tomograms which are 2D vertical sections of the 3D focussed image.

The magnitude and the position of the dominant scattering contributions within the snow and ice layers are effectively identified by imaging the vertical scattering structure of the snow-ice-water complex medium. This information has helped to improve our understanding of the interaction between microwaves and snow and ice layers. In our study, it is found that scattering

contributions at the interfaces within the air-snow-ice-water complex medium are more dominant than the corresponding volumetric contributions within the snow and ice. Moreover, comparisons of the strength of the scattering contributions of the snow and ice volumes at both test sites reveal that, in most cases, the ice volume contribution is stronger than that of the snow volume. This is attributed to the abundance of air bubbles which are irregularly shaped and randomly oriented throughout most of the ice volume. The presented results reveal that in a snow-ice-water complex medium, the backscatter response is a cumulative effect of the small scale roughness of the interfaces between the different layers, and the dielectric discontinuity caused by inhomogeneities within the snow and ice volumes, with the contribution of the ice layer being much higher than that of the snow.

Radar waves experience a change in speed and direction upon propagating through a multilayer dielectric medium. It is found that ignoring this effect during tomographic SAR data focusing causes distortion of the information in the tomograms and complicate the interpretation of the results. A rigorous mathematical formulation which accounts for this refraction phenomenon in a multi-layer medium is presented and used as a basis for estimating the depths and the refractive indices of snow and ice layers through an optimization procedure. The estimated depths are compared with measured ones and a good agreement is found.

Characterization of natural media through tomographic SAR imaging can be improved through the use of multiple frequencies and polarizations. The electromagnetic responses of snow and ice are investigated and compared at VV and HV polarizations. The results reveal that the HV response of the ice layer is remarkably stronger than that of the snow layer. This is associated to the depolarizing capability of irregularly shaped and randomly oriented air bubbles in the ice layer. It is also observed that the VV response of the observed medium is stronger than the corresponding response at HV.

Moreover, the vertical structure of the reflectivity of the snow covered lake ice is investigated and compared at X-, and C-band. Results reveal that the volume contributions of the snow and ice layers are very weak at C-band compared to that of X-band. The results also show that the C-band interface responses are remarkably stronger than the corresponding volumetric responses. Moreover, the response of the interfaces at C-band is limited to small incidence angles compared to that of X-band. This is explained to be attributed to the difference in the two wavelengths with respect to the scale of surface and volume scattering features.

The second part of the thesis which is presented in paper III, focuses on

the retrieval of the local surface topography of landfast multi-year sea ice in the Fram Strait, located close to the east coast of Greenland, using an interferometric dataset acquired by TanDEM-X. Datasets acquired from helicopter-borne stereo camera and laser profiler are used to evaluate the performance of interferometric sea ice surface height retrievals over an 8 km long segment. Results reveal that 80% of the ridges with height values greater than 0.5 m can be estimated with a root-mean-squared-error which is less than or equal to 0.3 m, with the relative error decreasing significantly as a function of ridge height. The results also show that the topographic information derived from one-dimensional laser altimeter profiles can be well used to validate the interferometric height maps when the width of the ice surface structures are comparable to or larger than the size of the averaging window used for interferometric processing. Complementary information which supports the comparison between the different measurement instruments is obtained by investigating sea ice ridge statistical features such as the number of detected ridges, the maximum, minimum, and average heights of the individual ridges. The need for multilook averaging to reduce phase noise as well as the presence of open or refrozen leads are identified as the main challenges when it comes to the use of SAR interferometry for sea ice topographic height retrieval.

This thesis contributes to an improved understanding regarding the potential of SAR tomography for imaging the vertical scattering distributions of snow and ice layers, and for studying the influence of both sensor parameters such as its frequency and polarization and scene properties such as layer stratification, air bubbles and small-scale roughness of the interfaces on snow and ice backscattered signal. Moreover, the work reveals the potential of SAR interferometry for retrieving the surface topography of sea ice.

Acknowledgments

I am pleased to acknowledge the people who helped and inspired me throughout my doctoral study. First and foremost, my deepest gratitude goes to my supervisors Torbjørn Eltoft and Laurent Ferro-Famil for tirelessly working, and sharing their broad knowledge and experience with me. Torbjørn, I am very grateful to you for giving me the opportunity to study an interesting research topic, for your helpful suggestions, encouragement and patience. Laurent, I am deeply indebted to you for all the important things you taught me, helped, encouraged and hosted me at your laboratory, IETR at the University of Rennes 1, France. It is an honour working with you.

I would also like to acknowledge the many scientists who have been involved in my research, and are featured as co-authors in my papers. Stefano Tebaldini, Wolfgang Dierking, Dmitry V. Divine, Anja Rösel and Jean Negrel, thank you all for your contributions and it has been a great pleasure working with you. Moreover, I would like to thank Cécile Leconte and Frédéric Boutet for your contributions during the data collection process. I would also like to acknowledge the polar institute and members of the Fram Strait 2016 campaign for organising a successful campaign and providing me in situ measurements for my third paper.

I would like to thank the rest of the Earth observation group members, Camilla Brekke, Anthony P. Doulgeris, all the post docs and former and current PhD fellows. It has been a pleasure working with you and thank you for the wonderful time.

I would also like to take this opportunity to thank the rest of the IETR laboratory group members, Eric pottier, the engineers, post docs and PhD students for the wonderful working environment and making my time at the lab enjoyable.

Finally, my sincere gratitude goes to my family and friends who supported, encouraged and inspired me from the beginning until the end.

Temesgen Gebrie Yitayew

Tromsø, November, 2017

Contents

Nomenclature

List of Notation

$a_{m,n}$	antenna position at elevation m, and azimuth n acquisition positions
B	transmitted bandwidth
$B_\perp$	perpendicular baseline
c	speed of light
d	thickness of snow and ice layers or sublayers
d_n	Baseline in the normal direction
f_c	carrier frequency
f_e	flat earth contribution to the interferogram
h	local topography of the ice surface
H	Operating altitude of the SAR platform
H_v	height ambiguity
k	wave number
L_θ	the dimension of the real antenna in elevation
L_ϕ	the dimension of the real antenna in azimuth
L_z	synthetic aperture length in the elevation direction
L_n	synthetic aperture length in the normal direction
L_x	synthetic aperture length in the azimuth direction
M	total number of acquisitions in a tomographic SAR setup
N	total number of acquisition positions that form the azimuth aperture

N_L	number of looks for interferogram generation
n_i	refractive index of the i^{th} layer in the snow and ice
$\mathbf{n}$	the normal direction in a tomographic configuration
R_x	receiving antenna
$\mathbf{S}$	scattering matrix
T_x	transmitting antenna
θ	incidence angle
τ	propagation delay
τ_0	propagation delay in vacuum
λ	wavelength
δ_p	penetration depth
ϵ	complex dielectric constant
ρ	complex reflectivity
δ_x	azimuth resolution
δ_r	slant range resolution
δ_y	ground range resolution
δ_n	normal resolution
δ_z	vertical resolution
γ	interferometric coherence
γ_c	complex interferogram
$\sigma^2_{\Delta\phi_{\gamma_c}}$	phase variance or phase noise
σ_h	height standard deviation or height error

List of Acronyms

CR	coherence ratio
DEM	digital elevation model
EM	electromagnetic
FMCW	Frequency Modulated Continuous Waveform
GB-SAR	ground-baser synthetic aperture radar
IDFT	Inverse Discrete Fourier Transform
IETR	Institute of Electronics and Telecommunications of Rennes at University of Rennes 1
PoSAR	Pocket Synthetic Aperture Radar
PolInSAR	Polarimetric Synthetic Aperture Radar Interferometry
RMSE	root-mean-squared-error
SAR	synthetic aperture radar
SLC	single-look complex
SNR	signal-to-noise ratio
SFCW	Stepped Frequency Continuous Waveform
TDBP	Time Domain Backprojection
TomoSAR	Tomographic Synthetic Aperture Radar
VNA	vector network analyzer
2D	two-dimensional
3D	three-dimensional

Chapter 1

Introduction

The focus of this thesis is imaging in the vertical direction of different types of ice in arctic and sub-arctic regions. Specifically, the first part of the thesis focuses on tomographic imaging and on the characterization of snow covered fjord and lake ice, and the second part concentrates on the investigation of the local topography of sea ice surface using synthetic aperture radar interferometry. This chapter presents the motivations for the study and the outline of the thesis.

1.1 Motivation

Characterization of sea ice and its snow cover plays a pivotal role in understanding and monitoring changes in the global climate and ecosystem. The physical and electrical properties of the ice and its snow cover control the amount of solar radiation reflected to the atmosphere, absorbed within snow and ice, and transmitted into the ocean beneath the ice. Moreover, the topography of the sea ice surface affects the interaction between the atmospheric boundary layer and the sea ice cover [Garbrecht et al., 2002].

Synthetic aperture radar (SAR) is a coherent imaging technique which provides high resolution two dimensional (2D) images of the earth's surface by simulating a "big antenna", conventionally called synthetic aperture, using the motion of the acquisition platform and advanced signal processing techniques. Owing to its high resolution capability, and its ability to operate day and night, and under almost all weather conditions, SAR has been successfully applied for

virtually all remote sensing applications including sea ice, forest, urban, and ocean remote sensing. It operates at microwave frequencies, where some of the common ones being designated as X-, C-, L-, and P-band. The multi-frequency imaging capability combined with its ability to preserve the phase of the measured signal and operate at different polarization channels makes SAR a very powerful remote sensing tool for characterizing the imaged medium in terms of its geometric and electromagnetic properties. A SAR sensor can be mounted on ground-based vehicles, airborne and spaceborne platforms.

Satellite-borne SAR remote sensing is a widely used technique for large scale monitoring and studying of sea ice. Sea ice images acquired by SAR systems mounted on satellites have been used for a number of applications such as identifying different ice types and retrieving different geophysical properties such as sea ice concentration, surface morphology and ice texture [Kwok et al., 1992], [Aldenhoff et al., 2016], [Onstott, 1992], [Barber et al., 1992], [Soh and Tsatsoulis, 1999], [Moen, 2014], [Li and Perrie, 2016].

However, the characterization of semi-transparent volumetric media such as snow and ice using conventional 2D SAR imaging has serious limitations, as the radar signal penetrates to some degree into the volumes, and the recorded echoes are the result of the interaction between the wave and the complex three-dimensional medium. Due to its intrinsic 2D imaging nature, the conventional SAR imaging technique can not separate the scattering contributions (within a 2D resolution cell) in the vertical direction. Therefore, the characterization of the vertical layering structure and the analysis of the local distribution of the scatterers in snow and ice requires the use of imaging techniques that describe these complex volumetric media in a three-dimensional (3D) space. Multibaseline SAR techniques such as SAR tomography and SAR interferometry offer the possibility of retrieving information about the imaged medium in the vertical direction. Across-track interferometry uses the phase difference between at least two SAR images acquired from a unique configuration to derive the mean topographic height information of each resolution cell [Graham, 1974], [Zebker and Goldstein, 1986]. On the other hand, SAR tomography is the extension of conventional 2D SAR imaging to three dimensions, and offers the possibility of imaging the whole 3D scattering distribution of volumetric media [Reigber and Moreira, 2000]. Therefore, both across-track interferometry and SAR tomography can be considered as extensions of the conventional 2D SAR imaging for acquiring information about the observed medium in the vertical direction.

This thesis investigates 3D imaging of different ice types. The work consists of two closely related components. The first one is tomographic imaging

of fjord and lake ice using a ground based SAR system operated at different frequencies and polarizations. The system was built and operated by a team from the University of Rennes 1, France. The tomographic experiment was conducted on two different ice types, namely fjord ice collected over Kattfjord, and lake ice collected over Prestvannet lake, both in Tromsø area, in the northern part of Norway. The two test sites contain snow covered seasonal ice. The thickness of the snow and ice layers at both test sites were about a few tens of centimeters. The second component of this thesis deals with investigation of the local topography of sea ice using SAR interferometry from TanDEM-X. The area investigated is the Fram Strait, located between Greenland and Svalbard. The thesis investigates different ice types such as fjord ice which can be considered as low salinity sea ice, lake ice and multiyear sea ice. Therefore, the term "sea ice" in the title of the thesis is used in a more general sense. The main contributions of this work are organized in three papers. The first two are based on the tomographic SAR experiment, and the last one is based on the interferometric SAR experiment. The main objectives of the research are formulated as follows.

- Demonstrate the important potential of coherent 3D imaging in providing information about the snow and ice complex medium such as the number and location of the main contributions that cannot be accessed through 2D SAR imaging.
- Investigate the effect of the change in propagation velocity of the radar waves inside the volume in tomographic SAR imaging.
- Investigate the potential of SAR tomography for snow and ice parameter retrieval.
- Investigate the contribution of the different scattering mechanisms in the focussed tomographic SAR data.
- Investigate and compare the vertical structure of the radar reflectivity of the snow plus ice complex medium at two different polarization channels, VV and HV, and at two different frequencies, X-, and C-band.
- Investigate the local surface topography of sea ice using SAR interferometry and compare the results with equivalent surface topographic height values derived from helicopter-borne laser altimeter and stereo camera measurements.

Since its practical demonstration in [Reigber and Moreira, 2000], the technique of tomographic SAR imaging has been applied for forest, urban area, and very recently snowpack and glacier applications. [Reigber and Moreira, 2000], [Tebaldini and Rocca, 2012], [Reale et al., 2011], [Tebaldini and Ferro-Famil, 2013], [Banda et al., 2016], [Tebaldini et al., 2016]. However, to the best of our knowledge, no published works are available regarding 3D imaging of sea ice employing 2D synthetic arrays. Moreover, the issue of topographic retrieval of the earth's surface using SAR interferometry is not new [Graham, 1974], [Zebker and Goldstein, 1986], and is a well established technique for Digital Elevation Model (DEM) generation [Rufino et al., 1998], [Werner, 2001]. However, sea ice surface topographic retrieval using SAR interferometry from space has gotten more attention only very recently after the introduction of single-pass satellite interferometers that can image the polar regions [Scheiber et al., 2011], [Dierking et al., 2017]. In other words, published studies on the topic of sea ice topographic retrieval using SAR interferometry from space are also scarce [Berg et al., 2015]. Therefore, the research in this thesis is intended to contribute in filling these gaps.

1.2 Outline of the thesis

Following this introduction, chapter 2 briefly introduces the concept of SAR imaging. Chapter 3 introduces 3D imaging using SAR techniques such as SAR interferometry and SAR tomography. Chapter 4 reviews the properties of sea ice and the mechanisms through which it interacts with EM waves. Special attention is given to the physical and electrical properties of the sea ice relevant to microwave scattering. Chapter 5 briefly introduces the test sites, experimental setup and data collection. A brief summary of the three publications and the corresponding key research contributions are presented in chapter 6, whereas the full papers are presented in chapters 7-9. Finally, conclusions and outlook are presented in Chapter 10.

Chapter 2

Basics of SAR imaging

This chapter provides a brief overview of the conventional SAR imaging technique. Details about SAR imaging can be found in many text books and review tutorials such as [Curlander and McDonough, 1991], [Soumekh, 1999], [Cumming and Wong, 2005], [Franceschetti and Lanari, 1999], [Tomiyasu, 1978], [Moreira et al., 2013]

2.1 Operating principle and geometry

SAR is an imaging radar system that can be mounted on a moving platform and provides high resolution 2D images of the earth's surface. It utilizes the motion of the platform to synthesise a *long virtual antenna* through advanced signal processing techniques. Unlike optical sensors, which depend on naturally available energy sources, SAR transmits its own illumination and can operate day and night in the microwave region of the EM spectrum. It is hence capable of acquiring images independent of clouds and weather conditions. As a result of these qualities, SAR has been an important remote sensing tool for numerous disciplines and applications such as geoscience and earth system monitoring, 2D and 3D mapping of the earth's surface, climate research, and surveillance. Depending on the platform that carries the radar system, the swath width (see Fig. 2.1) can vary from a few meters for ground-based systems to tens of kilometres for spaceborne systems. Ground-based SAR is mainly used for fine scale mapping and *in situ* data collection, airborne platforms are preferred for intermediate scale mapping as well as for demonstrat-

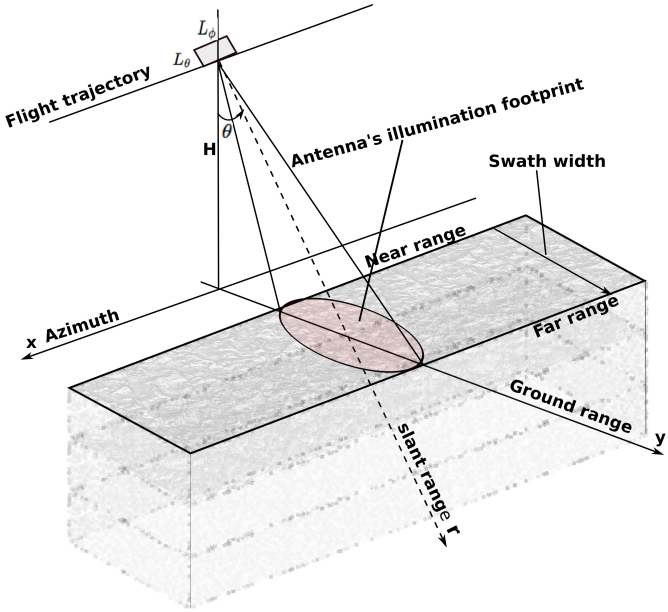

Figure 2.1: Side-looking geometry of a conventional SAR system, imaging a multilayer complex medium. Figure adapted from [Lee and Pottier, 2009].

ing the feasibility of new remote sensing techniques and applications that can later be implemented in spaceborne SAR missions, and satellite-based SARs offer regular monitoring on a global scale. In particular, satellite-based SAR is very useful for monitoring arctic sea ice, where access is generally limited by harsh weather conditions in the polar regions.

The side-looking acquisition geometry of SAR is shown in Fig. 2.1. This geometry corresponds to the commonly used acquisition mode of SAR called *strip map*. The flight direction is called azimuth, and the antenna pointing direction, which is perpendicular to the flight trajectory, is called slant range. L_θ and L_ϕ are the dimensions of the real antenna in elevation and azimuth directions, respectively, and θ is the look angle. The point on the ground directly below the platform position ($\theta = 0$) is called nadir [see Fig. 2.2(a)]. The extent of the imaged scene in the range direction is called swath width, and its edge closest to nadir is called near range, whereas the one farthest from nadir

is called far range. As the platform advances along its trajectory, the radar system periodically transmits electromagnetic pulses into the illuminated footprint and records the backscattered echoes coherently.

The recorded signal (also called SAR raw data) is usually arranged in a 2D matrix, one of the coordinates being the two-way signal delay and the other being the pulse number, which can be translated into the sensor position in the azimuth direction. Due to the fact that a given target's response is "distributed" over many pulses, the raw data are not suitable for direct interpretation of the measured targets. The process of transforming the raw data into a SAR image is called focusing. Commonly used SAR focussing algorithms include *range-doppler* [Munson and Visentin, 1989], *chirp scaling* [Raney et al., 1994], [Moreira et al., 1996], *Omega-k* [Cafforio et al., 1991], and *time domain back projection* algorithms [Ulander et al., 2003]. After focusing, the value of each pixel in the SAR image represents the complex reflectivity of all the targets in the corresponding resolution cell.

2.2 Resolution and frequency bands

Resolution refers to the smallest separation between two adjacent point targets that can be resolved by the radar system. As it is pointed out at the beginning of this section, SAR is a 2D imaging system, and therefore its resolution has two components, in the azimuth and range directions. The slant range resolution is a function of the transmitted bandwidth and is given by

$$\delta_r = \frac{c}{2B}, \tag{2.1}$$

where B is the bandwidth in Hz of the transmitted pulse and c is the speed of light in vacuum in $^{m}/_{s}$.

The resolution component in the ground range direction δ_y is approximately related to the slant range resolution by $\delta_y = {}^{\delta_r}/_{\sin\theta}$ implying that the ground range resolution varies nonlinearly across the swath width. Equation 2.1 implies that resolution improvement in the slant range direction can be achieved by transmitting pulses with wide-bandwidth or short pulse length (as the two are related by $B = {}^{1}/_{\tau}$, where τ is the pulse length). However, short pulses are associated with low signal energy which is undesirable as it limits the detection ability of the SAR system [Curlander and McDonough, 1991]. This dilemma in SAR systems is remedied by transmitting either Linear Frequency Modulated pulse Waveforms (LFM) or Stepped Frequency Con-

tinuous Waveforms (SFCW) [Wehner, 1987]. In LFM SAR systems, a relatively long pulse, whose frequency varies linearly with time over the bandwidth (also called *chirp*), is transmitted, and pulse compression techniques are employed at the reception end to achieve wide-bandwidth and high average transmitted power simultaneously. On the other hand, a SFCW SAR system constructs its wide-bandwidth signal by transmitting, at each sensor position, a group of narrow-band pulses, stepped at a fixed frequency step-size over the desired bandwidth. Signal processing techniques such as Inverse Discrete Fourier Transform (IDFT) are employed to construct the wide-bandwidth signal [Wehner, 1987], [Lord, 2000]. This type of waveforms are used in ground-based and airborne SAR systems. Advantages of SFCW over LFM include high dynamic range and flexibility of improving the Signal-to-Noise ratio (SNR) of the system [Lord, 2000]. As it is discussed in **Papers I** and **II**, the experimental tomographic SAR system used in this study employs a SFCW waveform, and the datasets are collected at two frequency bands, X-, and C-band. Table 2.1 lists the commonly used bands in SAR systems. In general, it can be stated that longer wavelengths penetrate deeper into semi-transparent media such as snow and ice than shorter wavelengths. Details regarding the penetration depth of microwaves into snow and ice are presented in chapter 4.

Table 2.1: Frequency bands that are commonly used by SAR systems [Moreira et al., 2013].

Frequency Band	**Ka**	**Ku**	**X**	**C**	**S**	**L**	**P**
Frequency (GHz)	40-25	17.6-12	12-7.5	7.5-3.75	3.75-2	2-1	0.5-0.25
Wavelength (cm)	0.75-1.2	1.7-2.5	2.5-4	4-8	8-15	15-30	60-120

The azimuth resolution is a function of the synthesized aperture in the azimuth direction. The construction of the virtual aperture from the motion of the platform is illustrated in Fig 2.2(b). The process requires the coherent combination of the received echoes from a given point target while it remains in the main beam of the antenna, and the extent of the acquisition positions along the flight trajectory is the synthetic aperture. Denoting the synthetic aperture length in the azimuth direction by L_x, the azimuth resolution is given by

$$\delta_x = \frac{\lambda r_0}{2L_x}, \tag{2.2}$$

where λ is the wavelength and r_0 is the slant range. In strip map acquisi-

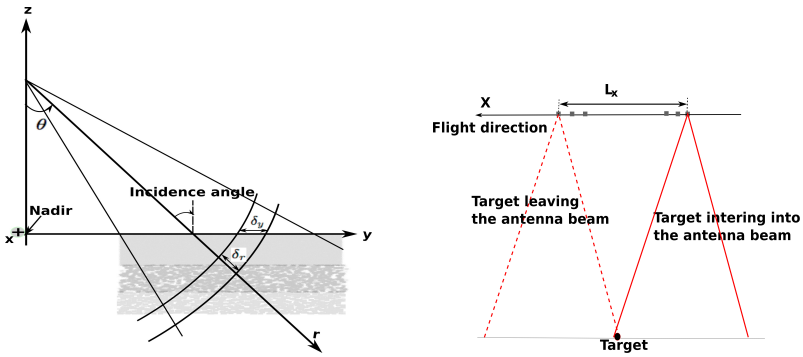

(a) (b)

Figure 2.2: Side-, and front-views of the side-looking geometry of SAR. (a) Side view showing more definitions associated to the 2D SAR acquisition geometry (b) Front view showing aperture synthesis in the azimuth direction.

tion mode with a full synthetic aperture being used for image formation, this resolution is approximately equal to half of the length of the real antenna in azimuth, i.e., $\delta_x \approx \frac{L_\phi}{2}$. This shows that the azimuth resolution is independent of the flight altitude, which makes SAR a powerful tool for high resolution mapping of the earth's surface from space. Today, spaceborne SAR systems are capable of acquiring images down to one meter resolution [Krieger et al., 2007]. Airborne and ground based SAR systems can achieve resolution of a few centimeters [Cantalloube and Dubois-Fernandez, 2006], [Yitayew et al., 2017].

2.3 SAR polarimetry

Polarization in EM waves refers to the trajectory of the electric field in a plane orthogonal to the direction of propagation. In addition to the wavelength, the polarization of the transmitted signal is another wave property that influences the interaction between the radar signal and the imaged medium. Depending on their shape, orientation, dielectric properties, illumination and scattering angles, targets exhibit a unique scattering behaviour for a given transmit-receive polarization combination [Cloude, 2009], [Ulaby and Long, 2014]. SAR polarimetry takes advantage of this fact to increase the observation space and consequently achieve improved characterization of targets. Consider an incid-

ent (transmitted) plane wave $\mathbf{E}_i$ with its orthogonally polarized components designated by $E_{p,i}$ and $E_{q,i}$. Upon interaction with a given target, the corresponding scattered field $\mathbf{E}_s$ with components $E_{p,s}$ and $E_{q,s}$ can be related to the incident one as follows [Lee and Pottier, 2009]:

$$\begin{bmatrix} E_{p,s} \\ E_{q,s} \end{bmatrix} = \left(\frac{e^{-jkr}}{r} \right) \begin{vmatrix} S_{pp} & S_{pq} \\ S_{qp} & S_{qq} \end{vmatrix} \begin{bmatrix} E_{p,i} \\ E_{q,i} \end{bmatrix}, \tag{2.3}$$

where r is the range from the object to the receiver, and $k = \frac{2\pi}{\lambda}$ is the wavenumber.

In short hand form, Eq. (2.3) can be written as $\mathbf{E}_s = \left(\frac{e^{-jkr}}{r} \right) \mathbf{S}\mathbf{E}_i$, where $\mathbf{S}$ is called the scattering or Sinclair matrix. It characterizes the scattering behaviour of the object for the four possible combinations of the p- and q-polarization components. The four elements of $\mathbf{S}$ whose first and second subscripts refer to the polarization of the scattered and transmitted fields, respectively, are called scattering amplitudes and are in general complex values.

In the linear horizontal (H) and vertical (V) polarization basis representation with p=H and q=V, $\mathbf{S}$ has the following form:

$$\mathbf{S} = \begin{vmatrix} S_{HH} & S_{HV} \\ S_{VH} & S_{VV} \end{vmatrix} \tag{2.4}$$

Depending on its polarization capability, a given SAR system can record one, two or all of the components of $\mathbf{S}$. SAR systems that transmit and receive at a single polarization channel are called *single polarized* or single-pol SAR systems. A SAR system that can record two polarization channels is called *dual polarized* or dual-pol system. In this case, a single transmitter and two receiving channels, or two transmitting and two receiving channels can be used. If a system is capable of recoding all the four possible combinations, it is called *fully polarized* or quad-pol SAR system.

2.4 Some properties of SAR images

Due to their relevance to the remaining part of the thesis, it is important to briefly discuss some of the unique characteristics of SAR images, such as *speckle* and *geometrical distortions*, before advancing to the next chapter.

Speckle

Distributed targets are characterized by the presence of many elementary scatterers that are randomly distributed throughout the medium. As it is discussed above, SAR is a coherent imaging system, and the coherent summation of the scattering contributions of these elementary scatterers within a resolution cell results in variations of the resultant amplitude and phase values from pixel to pixel. This variation manifests itself as a "salt and paper" appearance in SAR images and is known under the name of "speckle" [Goodman, 2007]. Statistical characterization of the intensity and phase information of SAR images is discussed in detail for example in [Oliver and Quegan, 2004], [Lee and Pottier, 2009]. Speckle causes the measured information to have a higher variance. Therefore, it often complicates image interpretation and parameter retrieval from SAR images. Its effect can be reduced by averaging over neighbouring pixels, a technique commonly known as *multilooking*. Even though multilooking reduces the variance and often improves image interpretability, it degrades the spatial resolution of SAR images. The effect of multilooking on the retrieved parameters using the interferometric SAR technique is discussed in **Paper III**.

Geometrical distortions and limitations of SAR for volumetric imaging

Another group of properties arising from the side looking geometry of SAR are geometrical distortions. The three common geometrical effects discussed in the literature are foreshortening, shadowing and layover. More details regarding SAR geometrical distortions can be found in [Stiles et al., 1982], [NRCAN, 2015]. Foreshortening refers to a situation where the extent of an imaged area appears smaller in the SAR image than its actual size. This can occur for example, when the antenna beam reaches the base of a tall mountain which is tilted towards the radar before it reaches the tip of it. Shadowing refers to the presence of relatively dark regions in the image due to the fact that the area can not be illuminated by the radar beam (for example the side of the mountain facing away from the radar). On the other hand, layover in general refers to the misrepresentation of the imaged features of a given medium. In the context of imaging a terrain with big topographic features such as high mountains, layover occurs when the tip of the mountain is imaged before the base, and appears displaced toward the radar. In the case of topographic features with very high slopes, layover refers to the distortion of the position and reflectivity information of many terrain patches which are equidistant from the sensor but

located at different elevation angles [Lombardini et al., 2003].

In the context of semi-transparent volumetric media such as snow, ice and forest where the penetration of the transmitted signal is significant, layover occurs due to the fact that all the scattering contributions of the volume are misrepresented as they are projected on a 2D azimuth-slant range plane. Referring to Fig. 2.2, the curved structure represents the cross-section of an azimuth-slant range resolution cell of a multilayer volumetric medium in the elevation-slant range plane. In the 3D space, it is a curved cylinder, however, all the contributions inside this volumetric cylinder will be projected onto a 2D azimuth-slant range plane. In other words, even though the penetration capability of microwaves offers the opportunity to "see" inside the volume, the information is misrepresented or lost during the 2D planar representation. Therefore, the conventional 2D SAR configuration is not capable of separating scattering contributions in the vertical direction. This refers to both the magnitude and the vertical position of the individual scattering contribution in the volume. Therefore, in order to acquire information of such media in the vertical direction, alternative techniques have to be exploited. The rest of the thesis investigates the possibility of obtaining information about semi-transparent media such as snow and ice in the elevation direction using extensions of the conventional 2D SAR imaging technique, namely SAR interferometry and SAR tomography.

Chapter 3

3D imaging using single- and multi-baseline SAR techniques

This chapter provides a brief overview of 3D imaging using SAR techniques.

3.1 Across-track interferometry

The end of chapter 2 highlighted the limitation of the conventional 2D SAR configuration for acquiring the height information of targets or the scattering distribution of the targets in the vertical direction. The first adaptation of the SAR technique to acquire information in the vertical direction is across-track SAR interferometry (across-track InSAR). In general the InSAR technique uses the phase difference between two or more co-registered complex SAR images acquired from slightly shifted positions (or different times or both) to accurately estimate parameters such as surface topography, line-of-sight displacements of targets, and changes experienced by natural and man-made targets over time [Bamler and Hartl, 1998]. The technique has been demonstrated for a wide range of terrestrial applications including DEM generation [Ferretti et al., 1999], [Werner, 2001], [Rufino et al., 1998], [Rabus et al., 2003], monitoring natural hazards [Massonnet et al., 1993], [Hooper et al., 2004], [Amelung et al., 1999], and glacier movements [Rao et al., 2004], [Prats et al., 2009].

The conventional across-track InSAR technique is used to drive the surface topography of the imaged medium from the phase difference of two co-registered complex SAR images acquired from slightly shifted positions. This is possible due to the fact that the phase information of each pixel in a SAR image contains highly accurate range information, and therefore the phase difference between two SAR images can be used to measure very small path length differences. This path length difference can then be used to approximately derive the mean height information of the target. The acquisition geometry of the conventional across-track InSAR is shown in Fig 3.1. It consists of two SAR systems S_1 and S_2 moving along their own flight trajectories which are laterally displaced from each other. The distance separating the two antennas is called baseline and has a parallel and a perpendicular component with respect to the look-direction. The two SAR systems can be mounted on aircrafts or satellites. Such a configuration can be achieved either by flying two platforms in a synchronized flight path [Krieger et al., 2007], or putting two spatially displaced receivers on the same platform [Werner, 2001]. Such systems are called single-pass interferometers and are suitable for topographic mapping applications under short temporal decorrelation senarios. The two SAR systems can be operated either independently, where each transmits and receives its own pulses, or in such a way that only one of them transmits and both of them receive, i.e., *bistatic mode*. Another option to achieve a configuration similar to Fig. 3.1 is by repeatedly flying over the same area (while maintaining the lateral shift between the two flight paths) using a single instrument [Bamler and Hartl, 1998]. These ones are called repeat-pass interferometers. However, such configurations can be used for topographic mapping only if the scene remains unchanged during the acquisition period of the two datasets. For satellite acquisitions in particular, this assumption may not be valid as the scene might change significantly during the repeat-period of the satellite.

Referring to Fig. 3.1, a change in the topography of the imaged medium from P to Q by Δh induces a change in path length difference Δr, and the relationship can be approximated by [Hanssen, 2001]

$$\Delta r \approx \frac{B_\perp \Delta h}{r_1 sin\theta_1}, \tag{3.1}$$

where $B_\perp$ the perpendicular component of the baseline B, θ_1 is the local incidence angle, and r_1 is the slant range with respect to the master acquisition. Taking the product of the first SAR image and the complex conjugate of the second SAR image on a point by point basis produces a complex quantity known as *interferogram*, and if the two acquisition systems are operated independently,

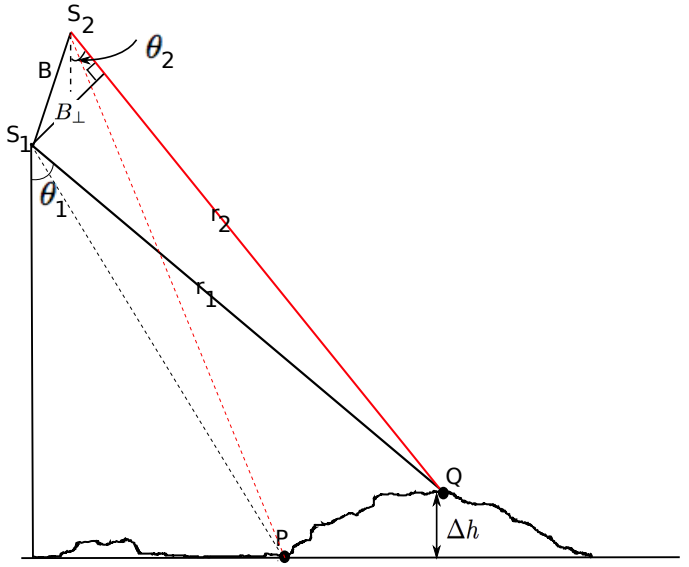

Figure 3.1: Geometry of across-track interferometry for topographic mapping.

the phase of the interferogram $\Delta\phi$ can be related to the path length difference Δr by:

$$\Delta\phi = \frac{4\pi}{\lambda}\Delta r, \tag{3.2}$$

where λ is the carrier wavelength. If a single transmitter is employed, only the one-way path is considered, and therefore the 4π in (3.2) should be replaced by 2π. As it can be noted from (3.1) and (3.2), by measuring the path length difference via the phase difference between the two acquisitions, the topography of the medium can be estimated. For the measured phase to be converted to topographic height maps, a number of preprocessing steps are required. These include image co-registration, interferogram generation, flat earth phase removal, interferogram filtering, phase unwrapping and phase-to-height conversion. Some of these preprocessing procedures, and additional mathematical expressions regarding the issue InSAR processing, are provided in **Paper III**. Detailed mathematical derivations can be found for example in [Hanssen, 2001].

The *interferometric coherence*, which is the magnitude of the complex correl-

ation coefficient computed over a local window, is a parameter used to measure the quality of the phase by quantifying the degree of signal decorrelation between the two acquisitions that form the InSAR pair [Rosen et al., 2000]. The main sources of signal decorrelation in InSAR pairs can be catagorized as spatial, temporal and thermal [Zebker and Villasenor, 1992]. The origin of the spatial decorrelation is the fact that the medium is imaged from two slightly different look angles (due to the spatial baseline) which in turn could result in different speckle behaviour. The temporal decorrelation is due to changes (on the scale of the wavelength) in shape, size orientation or position of the target as well as changes in the atmospheric constituents over the time window of the two acquisitions. The thermal noise is associated to the signal-to-noise ratio (SNR) of the system. The total decorrelation is given by the product the individual sources [Rosen et al., 2000], [Zebker and Villasenor, 1992]. For single-pass interferometers, the temporal separation between the acquisitions is very small compared to the decorrelation time of most media (water could be an exception), and therefore the effect of temporal decorrelation can be neglected. The decorrelation due to low SNR is a challenge in low backscatter areas such as calm water and smooth surfaces, and is deterrent to the use of the technique for media containing such structures.

Here, it is important to mention that there is a second category of well established InSAR application called along-track interferometry [Moccia and Rufino, 2001]. In this case however, the two SAR images are acquired with a certain temporal separation or with some along-track distance separation, and their phase difference is used to estimate the line of sight displacement of the observed targets. Techniques such as differential SAR interferometry and its variant Persistent Scatterer Interferometry belong to this group. However, the topic of line of sight displacement estimation using these techniques is outside of the scope of this thesis, and further details can be found, for example in [Gabriel et al., 1989], [Massonnet et al., 1993], [Ferretti et al., 2001].

One very important point to emphasize is that the height information estimated from across-track interferometry is the mean height corresponding to the scattering phase center of all the contributions within a given azimuth-range resolution cell. Therefore, this technique is suitable if the objective is to retrieve the mean surface topography of the observed medium. **Paper III** investigates the local topography of sea ice using this technique. However, if the desire is to acquire information about the scattering distribution of all targets in the vertical direction (under the assumption of reasonable penetration), the conventional across-track InSAR has limitations as it lacks the resolving capability in the elevation direction. In other words, the conventional across-track

InSAR does not satisfy the precise definition of 3D imaging. The next development in attempting to acquire the distribution of the scattering contributions in volumetric media is polarimetric SAR interferometry (PolInSAR) [Cloude and Papathanassiou, 1998], [Papathanassiou and Cloude, 2001]. This techniques combines the attributes of SAR polarimetry and SAR interferometry to characterize the vertical distribution of the scattering process in the volume. A single interferogram acquired at different polarizations or multiple interferograms from multi-baseline acquisition systems, also acquired at multiple polarization channels can be employed. However, the technique relies on physical models describing the observed volumetric medium, and the characterization of the vertical structure is pursued through the inversion of the considered model. Moreover, the number of scattering elements in a given resolution cell that can be identified by PolInSAR is limited due to the fact that the identification is based on their scattering mechanisms as characterized by the corresponding polarimetric responses. PolInSAR is also outside of the scope of this thesis, and further details can be found for example in [Cloude and Papathanassiou, 1998], [Papathanassiou and Cloude, 2001], [Cloude and Papathanassiou, 2003], [Krieger et al., 2005], [Tebaldini, 2009]. If the desire is to directly image and fully characterize the vertical scattering distribution of volumetric media such as snow, ice and forest, direct 3D imaging approaches are needed. SAR tomography is such a technique and represents the major part of the work in this thesis. It is introduced in the next section.

3.2 SAR tomography

As it is discussed in chapter 2, microwave frequencies are capable of penetrating deep into semi-transparent media and interact with the volume. This attribute can be exploited to characterize the volume and acquire information about the vertical distribution of the reflectivity. It is discussed in chapter 2 that the conventional 2D SAR imaging achieves resolution improvement in azimuth by synthesizing a long virtual aperture in the flight direction. The same concept of aperture synthesis can be utilized to achieve a similar resolution improvement in the elevation direction, and the technique is called SAR tomography (TomoSAR) [Reigber and Moreira, 2000]. Therefore, TomoSAR is the extension of conventional 2D SAR imaging to three dimensions, and is achieved by the formation of an additional synthetic aperture in the elevation direction.

The elevation aperture can be achieved by imaging the medium of interest

from multiple parallel tracks that are shifted in the elevation direction. The geometry of a general TomoSAR imaging system also called multibaseline InSAR configuration is shown in Fig. 3.2. In its most general form, it consists of M parallel tracks shifted by a spacing d_n along the *normal* direction designated by $\mathbf{n}$. The normal direction is orthogonal to both the slant range and azimuth coordinates. The total normal aperture L_n is the total baseline spanned by the parallel tracks. Note that, in Fig. 3.2(a), the parallel tracks are projected on the z-axis for ease of representation. In general, the baseline between two tracks can have any orientation, and the total normal baseline is the sum of the projections of the individual baselines onto the $\mathbf{n}$ axis. For example, the experimental ground-based SAR system used in this thesis has its total vertical aperture oriented along the z-axis. Details are provided in chapter 5 and **Papers I** and **II**.

From Fig. 3.2(a), it can be noted that the two synthesized apertures in the azimuth and elevation directions result in a 2D synthetic array. The coherent combination of the recorded echoes from this 2D aperture results in high resolution 3D images of the observed medium. Therefore, the TomoSAR technique provides a unique opportunity to acquire information about the vertical scattering distribution of volumetric media such as forest, snow, sea ice and glaciers. It was first demonstrated for forest vertical structure charactrization in [Reigber and Moreira, 2000]. More forest application examples include [Tebaldini, 2010], [Tebaldini and Rocca, 2012], and [Huang et al., 2012a]. Other application examples such as detection of objects hidden under foliage [Nannini et al., 2012], [Huang et al., 2012b], monitoring urban infrastructures, [Reale et al., 2011], [Zhu and Bamler, 2012] and snowpack characterization [Rekioua et al., 2016] can also be mentioned. **Papers I** and **II** investigate the application of the technique for snow covered fjord ice and lake ice imaging and characterization.

Similar to the the azimuth resolution in SAR, the vertical resolution in TomoSAR is a function of the elevation synthetic aperture. The Fourier resolution in the normal direction is given by [Reigber and Moreira, 2000]

$$\delta_n = \frac{\lambda r}{2L_n}, \tag{3.3}$$

where r is the slant range, and λ is the wavelength. For the geometry shown in Fig. 3.2, since a height in the vertical direction z and a height in the normal direction n are related to each other by $z = n \sin\theta$, the vertical resolution can be approximated by

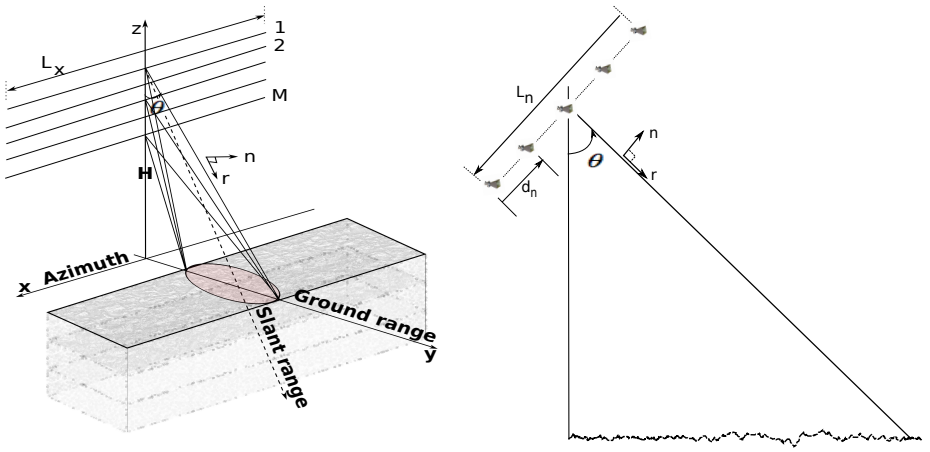

(a) (b)

Figure 3.2: Tomographic imaging geometry. (a) Geometry of a multilayer medium such as snow and ice. L_x is the azimuth aperture. Note that the parallel tracks are projected on the z-axis for ease of representation. In general, the baseline between two passes can have any orientation. (b) Representation of the normal total baseline (viewed from the flight direction). L_n is the total normal baseline or the synthetic aperture length in the normal direction. The normal direction is orthogonal to both azimuth and slant range directions.

$$\delta_z = \frac{\lambda r}{2L_n} \sin\,\theta, \tag{3.4}$$

Equations (3.3) and (3.4) imply that the vertical Fourier resolution can be improved by increasing the number of parallel tracks. However, achieving this is always a challenge as high number of parallel acquisitions complicates the design of tomographic SAR systems, specially in the case of spaceborne platforms [Moreira et al., 2013]. Another requirement in the design of tomographic SAR systems is the spacing between the acquisition tracks. To minimize the effect of side-lobes and avoid ambiguities in the elevation direction, the normal baseline should be formed from sufficiently sampled and regularly spaced parallel tracks. The regular spacing between the tracks in the normal direction, d_n, that fulfils the *Nyquist sampling criteria* is given by [Reigber and Moreira, 2000]

$$d_n \leqslant \frac{\lambda r}{2H_v}, \tag{3.5}$$

where H_v is the maximum height of the volume that can be reconstructed unambiguously. Equation 3.5 implies that smaller spacing between adjacent tracks results in larger height ambiguity. However this requires large number of tracks to keep the total baseline as large as possible. Therefore, for a given number of parallel tracks, a trade-off has to be made between the achievable vertical resolution and the unambiguous height that can be reconstructed.

Multibaseline configurations such as the one in Fig. 3.2 can be achieved by using ground-based, airborne and spaceborne platforms. However, it is important to point out that there are a number practical issues in all the three cases with respect to the number of parallel tracks, regular spacing among the tracks, signal focusing, and areal coverage. Fore example, a ground-based tomographic SAR setup can provide flexibility in terms of achieving several parallel acquisitions that are regularly spaced. However, it can only cover a small area and therefore can only be considered for experimental purposes. Similarly, airborne platforms are capable of acquiring data from several parallel flight tracks. However, achieving perfectly parallel tracks which are regularly spaced in the elevation direction is a challenge, and therefore motion compensation and calibration procedures are required [Reigber et al., 2013]. The use of satellites on the other hand for achieving several parallel tracks with near simultaneous acquisitions is a challenge, as flying several of them in close formation is extremely expensive. One possibility to achieve relatively high resolution tomography with the current operational satellites is via repeat-pass mode. However, temporal decorrelation is a big challenge, especially for sea ice which is a very dynamic medium. Moreover, the current operational satellites are designed to fly in a fixed orbital tube, and consequently the achievable vertical resolution is limited [Moreira et al., 2013]. In this thesis, a ground-based tomographic SAR system which will be introduced in chapter 5 is employed for data collection and form the basis of **Papers I** and **II**.

3.2.1 TomoSAR focusing

Referring to Fig. 3.2, the collected signal from the 2D synthetic array has to be focussed on a 3D space to produce 3D images. There are a number of approaches adopted for TomoSAR focusing, each motivated by various objectives such as resolution and accuracy improvements. One of the common approaches is by framing the issue of TomoSAR focusing as a spectral estimation

problem. In this category, 3D focusing is achieved in two steps. In the first step, the collected raw data from each of the M parallel tracks are focused independently using any of the 2D SAR focusing techniques mentioned in chapter 2 by synchronizing them to a common elevation position. Then, the 2D focussed signal from the m^{th} path at a given azimuth - slant-range position and the projections of the targets' reflectivity along the $\mathbf{n}$ direction form a Fourier transform pair [Reigber and Moreira, 2000], [Fornaro et al., 2003]. Consequently, both non-parametric spectral estimation techniques such as *Fourier* and *Capon* and parametric approaches such as *MUSIC* can be employed to retrieve the vertical reflectivity profile [Gini et al., 2002], [Lombardini and Reigber, 2003], [Gini and Lombardini, 2005]. Capon is called super-resolution technique as it is able to improve the resolution beyond the Fourier one given by (3.3). Another related approach for TomoSAR focusing which is also a supper-resolution technique is *compressive sensing* [Zhu and Bamler, 2009], [Zhu and Bamler, 2010a]. The technique is well suited for the reconstruction of irregularly sampled sparse signals, and therefore is well adapted to urban monitoring [Zhu and Bamler, 2012]. One of the issues associated with TomoSAR focusing using the techniques just mentioned is the geometric approximation made while computing the radar-scatterer distances of the M acquisitions by synchronizing them to a common single reference elevation position. This approximation can cause defocusing as it does not maintain the true geometric relationship between every acquisition position and the illuminated volume. For ground-based tomographic SAR configurations in particular, such an approximation can cause serious distortions as the variation in local incidence angles from one pass to the next may be significant.

A different approach than the ones mentioned above is the joint processing of the collected signal from the 2D array using the Time Domain Back Projection algorithm (TDBP) [Munson et al., 1983], [Frey, 2010]. This is a 3D matched filtering approach, and can be implemented through the use of the fast Fourier transform techniques (see **Paper I** for details). The TDBP focusing avoids the approximation pointed out above by directly computing the two-way radar-scatterer distances taking into account the geometric relationship between the sensor and the 3D scattering positions. Therefore, it is the most accurate approach for 2D and 3D SAR focusing. The TDBP approach is very convenient for airborne tomographic acquisitions where the flight paths in most cases are nonlinear [Frey, 2010]. The same is true for ground based acquisitions as it automatically takes in to account the changes in incidence angles from one pass to the next. The drawback of the TDBP focusing is that it is computationally slow, particularly for large images. However, the computational speed can be

improved through parallel computing, or at the expense of some phase accuracy [Ulander et al., 2003]. Moreover, for images acquired from ground-based systems, which are small in size, computational speed may not be a big issue. In TomoSAR, the focussed signal is usually presented as tomograms which are vertical sections of the 3D focused image. The TDBP focusing approach is applied for focusing the tomographic SAR data used in this thesis.

3.2.2 Further developments in SAR tomography

Two extensions of the conventional TomoSAR technique that can be mentioned here are *polarimetric SAR tomography* and *differential tomography*. In addition to the magnitude and position of the vertical reflectivity, these two variants of TomoSAR imaging can reveal information about the nature and the deformation of volumetric targets, respectively. Polarimetric SAR tomography exploits the polarimetric nature of the transmitted pulse to characterize the scattering process inside the considered volume [Guillaso and Reigber, 2005], [Tebaldini and Rocca, 2012], [Ferro-Famil et al., 2015]. Therefore, it can be used to either determine the nature of the imaged medium or highlight a specific scattering component in the volume. It has been mainly applied for forest vertical structure characterization [Tebaldini, 2010], [Tebaldini and Rocca, 2012], and [Huang et al., 2012a], and urban area applications [Huang and Ferro-Famil, 2009], [Sauer et al., 2011]. In **Paper I**, TomoSAR data acquired at two polarizations, VV and HV, will be used to investigate the volumetric response of snow covered fjord ice.

Differential tomography on the other hand exploits temporal diversity instead of polarimetric diversity to investigate the deformation velocity experienced by targets distributed in the vertical direction [Zhu and Bamler, 2010b], [Fornaro et al., 2010], [Reale et al., 2011], [Zhu and Bamler, 2012], [Fornaro et al., 2012]. However, the topic of differential tomography is outside of the scope of this thesis. Details can be found for example in [Lombardini, 2005], [Fornaro et al., 2014], [Fornaro et al., 2012].

Chapter 4

Physical and microwave scattering characteristics of sea ice

As it is pointed out in chapter 2, SAR systems acquire information about the imaged medium by transmitting microwave pulses and recording the backscattered signal. The backscattered signal is a function of the sensor parameters such as look angle, wavelength and polarization as well as of the properties of the observed medium. For sea ice, the backscattered signal depends on a number of parameters such as the surface roughness, the complex dielectric constant, the presence or absence of snow cover, and inhomogeneities within the snow and ice volumes. This chapter reviews some of the physical and electrical properties of sea ice that influence the interaction with microwaves. The objective is to provide a foundation that helps to understand the discussions made in the three paper regarding the interaction of the transmitted radar waves with the snow-ice-water complex medium during the 3D imaging process.

4.1 Physical and electrical properties of sea ice

Sea ice is a complex medium formed by freezing sea water. Sea water contains salts and gases dissolved in fresh water. As the temperature gradually decreases, the formation of ice crystals starts. The pure ice crystals make up the

lattice structure of the sea ice, whereas the dissolved salt is rejected in the form of liquid brine and form brine inclusions [Weeks and Ackley, 1986, Shokr and Sinha, 2015]. The gases form air bubbles. The brine inclusions and air bubbles will be trapped in between the ice crystals and coexist with the solid pure ice at equilibrium. The shape and concentration of brine inclusions and air bubbles trapped in sea ice are mainly dependent on the growth rate of the sea ice [Ulaby and Long, 2014]. As the ice ages, the liquid brine starts to drain as a result of mainly gravity drainage. This process creates empty brine channels. The air bubbles can then expand and fill in the void. This will ultimately result in large bubbles with irregular shapes. In addition to brine inclusions and air bubbles, sea ice may contain microalgae and precipitated solid salts [Shokr and Sinha, 2015]. Therefore, sea ice in general can be considered as a multiphase dielectric material. The dielectric property of a material characterizes the electrical behaviour of the material when subjected to electromagnetic fields. The dielectric constant ϵ of sea ice is in general a complex quantity with a real part, $\epsilon^{'}$, and imaginary part, $\epsilon^{''}$,

$$\epsilon = \epsilon^{'} - j\epsilon^{''}, \tag{4.1}$$

As ϵ is defined with respect to the dielectric constant of free space, it is also called the *relative dielectric constant* or *relative complex permittivity*. The real part, $\epsilon^{'}$, describes the refraction of the incident wave at the boundaries between two media or layers and how fast it propagates inside a dielectric volume. The imaginary part, $\epsilon^{''}$, also called the *dielectric loss factor* is linked to the attenuation of the wave. The dielectric constant of sea ice is a function the the dielectric properties of the aforementioned constituents as well as other parameters such as the volume fraction of each constituent [Hallikainen, 1992]. As these parameters are dependent on temperature and salinity, the dielectric constant is indirectly dependent on the temperature and salinity of sea ice [Ulaby and Long, 2014].

The real part of the dielectric constant and the real part of the refractive index, n, of any material are related through

$$n = \sqrt{\epsilon^{'}} \tag{4.2}$$

Throughout the thesis, n will be called *refractive index*. Estimation of refractive indices of the snow and ice layers using tomographic SAR data is presented in **Papers I** and **II**.

The spatial variability in size, shape, density and orientation of the aforementioned inhomogeneities in sea ice leads to ice stratification which results in

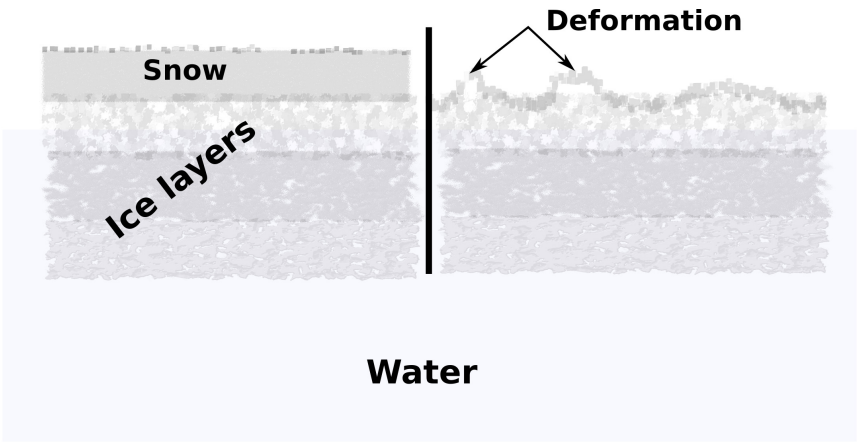

Figure 4.1: Demonstration of a multilayer stratified ice. The left part shows a snow covered ice and the right part shows deformation of the top surface of the ice with negligible snow cover.

distinct sublayers within the ice volume. The melting and refreezing of the ice volume in response to changes in temperature and weather conditions is also another factor for ice stratification. Adjacent sublayers in a stratified ice form an interface between them.

Sea ice can have snow deposits on top. Moreover, in response to changes in temperature and weather conditions over the period of the snow accumulation, the snow layer itself may develop sublayers. Therefore, sea ice in general can be considered as a multilayer medium that may contain multiple snow and ice sublayers floating on top of the sea water. Fig. 4.1 is a simple illustration of this multilayer nature.

Most of the above descriptions of sea ice are also valid for fresh water ice (formed from, for example, lakes and rivers), except the fact that it is not saline and consequently will not contain brine and brine channels.

As a result of ocean currents and winds, most of the sea ice is in constant motion and such ice is called *drifting sea ice*. The opposite is called *fast ice* which refers to immobile ice that is either fixed to the shores or grounded to the floor in relatively shallow waters. As a consequence of the drifting process and other factors such as changes in weather conditions, the top surface of the ice may undergo a complex deformation process. Depending on the driving forces of

the deformation process and the level of deformation, different terms such as *rafted ice*, *ridged ice*, and *hummocked ice* are used to identify the sea ice in terms of its surface structures [Onstott and Shuchman, 2004]. Rafted ice refers to a type of deformation where one piece of ice overlying on another, and mainly occurs in young ice. Sea ice ridges are formed as a result of compressional and shearing forces exerted on the ice cover. In general, ridges are complex deformation structures with a wide variability of sizes and shapes [Timco and Burden, 1997, Strub-Klein and Sudom, 2012]. Their dimensions in the vertical direction are defined with respect to the level water also called waterline. The height above the waterline is called *sail height* and the depth below the water line is called *keel depth* [Timco and Burden, 1997]. Hummocked ice refers to a smooth hill of ice that forms on the sea ice surface from eroded ridges, particularly during the summer melt [NSIDC, 2017].

The sea ice formation process passes through different stages of development and different names are commonly used for the different stages. A commonly used nomenclature developed by [WMO, 2014] classifies the entire stage into six groups according to age and thickness. These are *new ice, nilas, pancake ice, young ice, first-year ice*, and *old ice*. Details can be found in [WMO, 2014]. Ice types that have been growing for not more than one winter are called first-year ice. These types of ice develop from young ice and may have a thickness varying between 30 cm and 2 m. On the other hand, multi-year ice are old ice that have survived at least one summer melts and may have a thickness of 3 m or more. In **Papers I** and **II**, seasonal fjord ice, which can be considered as first-year low-salinity sea ice, is investigated, whereas in **Paper III** multiyear ice is investigated.

4.2 The nature of the interaction of microwaves with ice

Microwaves or EM waves in general interact with *natural dielectric media* mainly through *scattering* and *absorption*. From a physical point of view, scattering can be interpreted as follows. When an incident wave reaches the dielectric object, the electric charges inside the object are set into oscillatory motion. This motion of charges yield oscillatory currents, and these currents, in turn, radiate energy (similar to an antenna). These radiated waves constitute the *scattered* field. Therefore, in active remote sensing, often the objective is to radiate the object of interest with a wave, and acquire information about the object by

analyzing the scattered field. If the conductivity of a given material is not negligible, part of the incident wave can also be absorbed and lost in the form of other energies such as heat [Ulaby and Long, 2014].

For a multilayer complex semi-transparent volumetric medium of snow and ice (see Fig. 4.1), the backscatter signal is generally considered as a sum of several contributing backscattering responses. These are related to backscattering from air-snow, snow-ice, and ice-water interfaces as well as at interfaces between adjacent sub-layers within the snow and ice layers, and volume scattering contributions from the inhomogeneities within the snow and the ice layers [Carsey, 1992], [Ulaby et al., 1982b, Nghiem, 1991].

The relative strength of the backscatter power at the interfaces is dependent on the roughness of the surfaces with respect to the wavelength used, and the level of dielectric mismatch between the two media forming the interface. When the surface boundary separating two adjacent layers is perfectly smooth, the incident wave will be partly reflected into the specular direction and partly transmitted into the lower layer [see Figure 4.1 (a)]. As the surface gets rougher, the incident wave will be partly reflected in the specular direction and partly scattered in all directions [see Figure 4.1 (b)]. The specular component is often referred to as the coherent scattering component, whereas the scattered component is referred to as the diffuse or incoherent component. In the case of Fig. 4.1 (b), the magnitude of this diffused component is smaller than that of the reflected coherent component. As the surface becomes very rough, the coherent component becomes negligible [see Figure 4.1 (c)]. In statistical terms, the specular component represents the mean scattered field, whereas the diffuse component has a stochastic behaviour, associated to the randomness of the surface roughness. This randomness is characterized in terms of statistical parameters that are measured in units of wavelength. The two fundamental parameters commonly used are the *standard deviation of the surface height variation* (or *rms height*) and the *surface correlation length*. Such parameters describe the statistical variation of the random component of surface height relative to a reference surface. Details regarding the statistical description of rough surfaces can be found, for example, in [Ulaby et al., 1982a, Fung, 1994].

As it can be seen from Fig. 4.2(d), a portion of the incident wave also crosses the top boundary and interacts with the volume inhomogeneities. The relative strength of the volume return is a function of the dielectric contrast between the volume inhomogeneities and the background, the size (with respect to the wavelength), shape, orientation and correlations in positions of the inhomogeneities within the volume [Ulaby et al., 1982b, Nghiem, 1991].

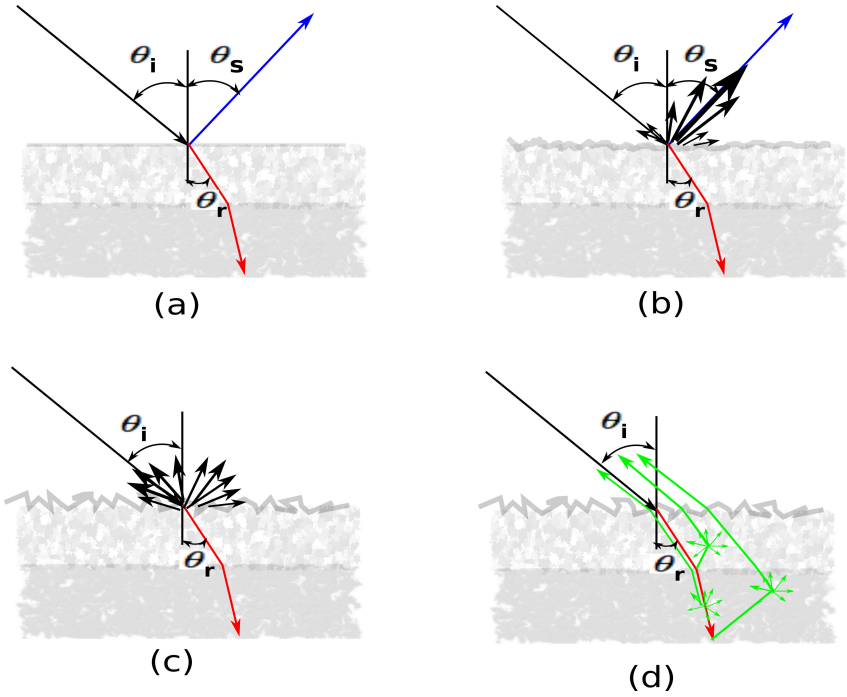

Figure 4.2: Interactions of microwaves with surfaces of varying roughness as well as volumes of multilayer media such as snow and ice. (a)-(c) show qualitative description of the relative contributions of coherent and diffuse scattering components for different surface roughness conditions where (a) is for specular, (b) is for slightly rough, and (c) is for very rough surfaces. The plots are adapted from [Ulaby et al., 1982a]. (d) shows a few of the many ways by which the transmitted signal interacts with volume inhomogeneities [Nghiem, 1991]. θ_i is the local incidence angle, θ_s is the scattering angle of the specular direction, and θ_r is the angle of refraction.

The effect of multiple scattering in TomoSAR imaging

One of the main assumptions in SAR imaging is linearity, i.e., the imaging process is assumed to be linear. This assumption models the imaged scene as an ensemble of dense point scatterers where the transmitted waveform interacts with these scatterers without multiple scattering and attenuation, and the

backscattered response of each resolution cell is obtained by linear superposition [Bamler and Hartl, 1998]. This assumption is equivalent to the first Born approximation in EM scattering modelling [Ulaby et al., 1982a]. However, in some volumetric media such as dense forest, snow and ice, multiple scattering is inevitable. In such cases, the above assumption can still be used, however, the reconstructed scene parameters correspond to the effective scattering centers within the resolution cell.

4.2.1 The influence of snow cover

The presence of snow on top of the ice surface influences the interaction of microwaves with the entire multilayered complex medium. Depending on its moisture content, a snow layer can be categorized as dry or wet. Dry snow is a mixture of ice and air, and therefore its dielectric constant is a function of the dielectric constant and the volume fraction of pure ice, which in turn is a sole function of snow density. Consequently, the real part of the dielectric constant of dry snow varies between 1 (for air) and 3.17 (for pure ice), with higher values correspond to very compact snow [Ulaby and Long, 2014]. Moreover, the size of the snow grains and the spacing between them which is filled by air is much smaller than many of the wavelengths used in SAR remote sensing. As a result, most microwave frequencies can penetrate through dry and relatively fresh snow without being significantly affected by the scattering process inside the snow volume. The exceptions are wavelengths smaller than or equal to X-band (see table 2.1), where the volume backscattering contribution from the snow layer may be non-negligible. As the snow ages and more fresh snow accumulates on top, the bottom part becomes compact. This process results in the formation of stratified snow layers where individual sublayers are characterized by different density, and hence different refractive indices [Rekioua et al., 2016]. Such stratification can also be formed as a result of melting and refreezing of sections of the snow volume as a result of thermodynamic processes [Birkeland, 1998]. The formation of such compact layers increases the backscattered signal from the snow volume at the aforementioned shorter wavelengths. Moreover, the presence of snow on top of the sea ice can influence the structure of the top surface of the ice. For example, in sea ice, either due to brine wetting [Crocker, 1992] or due to melting and refreezing of the top surface of the ice, the snow grains may stick to the surface and develop an artificial roughness or a coarse snow layer at the surface of the ice.

On the other hand, wet snow is a mixture of ice, air and liquid water. The liquid water content is quantified in terms of *snow wetness* which is the percent-

age of the volume fraction of liquid water in the snow mixture. The presence of liquid water which has a high dielectric constant compared to pure ice and air greatly affects the dielectric constant of the mixture. Water is a conductive material and if the snow is very wet, it becomes conductive and absorbent for most microwave frequencies. Consequently, waves can not penetrate and reach to the ice layer. In such circumstances, the reconstruction of the vertical reflectivity profile of the snow and ice layers using SAR tomography becomes impossible. The effect of penetration on 3D imaging using InSAR and TomoSAR techniques will be discussed in the next section. In summary, all the aforementioned snow properties affect the scattering process and therefore have to be taken into account when planning tomographic data collection campaigns as well as during data analysis.

4.2.2 The influence of penetration depth on 3D imaging of snow and ice

As it is pointed out in chapters 2 and 3, microwave frequencies are capable of penetrating into a semi-transparent volumetric media such as snow and ice and interact with the volume. However, along its path inside the volume, the transmitted wave experiences power lose due to volume scattering and absorption. The scattering losses are linked to redistribution of the energy of the transmitted wave into directions other than the refraction directions. The total power attenuation is usually referred to as extinction. The extinction per unit length is known as the *extinction coefficient*, and is given by the sum of the *scattering* and *absorption coefficients* [Ulaby and Long, 2014]. The penetration depth is the length along the propagation direction of the refracted wave at which the transmitted power falls to $\frac{1}{e}$. In other words, it represents the maximum depth within a given medium that contributes to the backscattering signal. It is given by the reciprocal of the extinction coefficient. However, as the scattering coefficient is often difficult to compute, the penetration depth is approximated by the reciprocal of the absorption coefficient [Ulaby et al., 1982a]. If the ratio of the imaginary and real part of the dielectric constant of the considered inhomogeneous medium is much smaller than one, i.e., if $\frac{\epsilon''}{\epsilon'} \ll 1$, then the penetration depth can be approximated by [Ulaby et al., 1982a]

$$\delta_p \approx \frac{\lambda\sqrt{\epsilon'}}{2\pi\epsilon''}, \tag{4.3}$$

where λ is the wavelength of the incident wave in free space. Such a me-

dium is called *low-loss dielectric* and snow and sea ice fall under this category [Ulaby and Long, 2014]. For a given medium, (4.3) implies that longer wavelengths are characterized by higher penetration depth than the shorter ones. Moreover, in addition to the wavelength, the dielectric constant determines how deep a given wavelength can penetrate into the snow and ice volumes. Typical penetration depth values reported in the literature for pure ice, multiyear sea ice and first year sea ice at X-band are about 10 m, 30 cm and 5 -10 cm, respectively [Ulaby and Long, 2014]. The corresponding reported values at C-band are about 70 m, 50 cm and 10 to 20 cm respectively. Therefore, in addition to the sensor parameters, the planning of a tomographic SAR data collection campaign should take into account the properties of the snow and ice volumes that one intends to observe.

The paradox of the effect of penetration in TomoSAR and InSAR imaging

Within the unambiguous limit of the volume that one is wishing to reconstruct [see (3.5)], TomoSAR relies on maximum penetration of the transmitted wave. However, it should be noted that the opposite is true for InSAR. In other words, when it comes to estimating the mean surface topography of the snow and ice layers using across-track InSAR, one would like to have as little penetration as possible. This is because, the speckle associated to the elementary scatterers inside the volume causes further degradation of the InSAR phase information. Whenever the penetration of the incident wave is significant in InSAR imaging, the spatial decorrelation will have two components; the surface and the volume decorrelation components. The effect of the surface decorrelation can be minimized using filtering techniques. However, this is not helpful to circumvent the effect of volume decorrelation as the elementary scatterers responsible for the speckle phenomenon in the volume are distributed in the vertical direction. Therefore, when there is significant penetration into the volume, the derivation of the expressions of the topographic parameters should be modified. In other words, the additional phase error due to the volume decorrelation needs to be taken into account for during the interpretation of the results. Details regarding the effect of penetration on sea ice topographic retrieval using the InSAR technique can be found in [Dierking et al., 2017].

Finally, it is important to mention that as the incident wave crosses a given boundary and propagates inside the lower volume, it refracts, i.e., it experiences a change in speed and direction. Therefore, in TomoSAR focusing, distance computation inside the snow and ice layers should consider this change.

The refraction phenomenon also results in changes in wavelength and incidence angle in the lower layers. Therefore, the interpretation of the 3D information should take into account these effects.

Chapter 5

Study areas, experimental setup and data sets

In this thesis, data collected during two different campaigns are used. The first is a dedicated tomographic SAR data collection campaign conducted on fjord and lake ice in the Tromsø area, north Norway. The datasets from this campaign form the bases for **Papers I** and **II**. The datasets used for **Paper III** are collected during a Fram Strait cruise campaign conducted in the Fram Strait region located close to the east cost of Greenland. This chapter provides a very brief overview of the datasets collected during these two campaigns. More detail descriptions can be found in the respective papers.

5.1 Tomographic SAR data acquisition

The tomographic SAR data collection campaign was conducted in March, 2013, by a team from the IETR, University of Rennes 1, France, in collaboration with members of the Earth Observation group at UIT, the Arctic University of Norway. A ground based tomographic SAR system is used to carry out the acquisitions at two different test sites.

5.1.1 Study areas

Kattfjord was one of the two test sites where the tomographic SAR data collection campaign was conducted. The fjord is located 40 km south west of Tromsø, Norway, and is connected to the Norwegian sea. The ice formed at the fjord is seasonal ice, and depending on the season, it can have a life varying between three and four months. Fig. 5.1(a) shows the map of the Tromsø area. The tomographic SAR measurements were carried out at the spot which is labeled as "Kattfjord test site". As it can be seen from the figure, the mouth of the fjord is farther away from the test site, and the fjord is surrounded by mountainous terrain. Due to fresh water flowing from the surrounding mountains during the early months of the winter, the water in the fjord was not as saline as an ordinary sea water, and consequently, the ice formed at the fjord was relatively fresh and can be considered as low salinity sea ice.

Fig. 5.1(b) shows a photographic image of the fjord. During the campaign, ancillary data such as the depth of the snow and ice layers, and photographs of the snow and ice layers are also acquired. The depth of the ice at the test site was about 28 cm, and that of the snow cover on top of the ice was about 24 cm. Fig. 5.3 shows some of the photos from the measuring process.

The second test site was Prestvannet lake. The lake is located at the middle of Tromsø island [see Fig. 5.1(a)]. The ice formed at the lake is also seasonal with a life of up to four months. The depth of the ice at the lake was about 90 cm, and that of the snow cover was about 20 cm. Table 2 summarizes the depths of the snow and ice layers at the two test sites.

Table 5.1: Summary of the depths of the snow and ice layers at the two test sites

Test cites	Depth of snow (cm)	Depth of ice (cm)
Kattfjord	24	28
Prestvannet lake	20	90

5.1.2 Experimental setup

The TomoSAR system used for data collection at the two test sites introduced above is a Ground-Based SAR (GB-SAR) system, named Pocket SAR (PoSAR), developed at the IETR, University of Rennes 1. Details of the system are given

(a) (b)

Figure 5.1: Test sites; (a) Map of the Tromsø area, in the northern Norway, and (b) a photograph of the test site at Kattfjord.

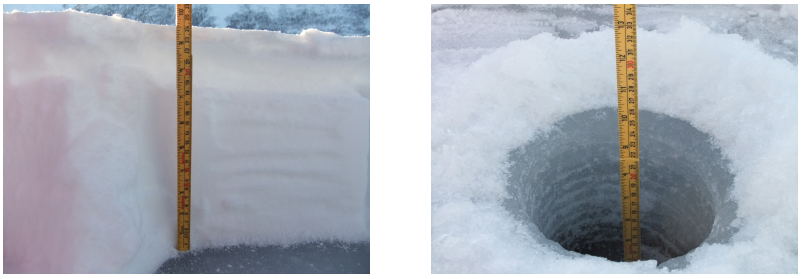

(a) (b)

Figure 5.2: Measuring the depth of snow and ice layers.

in **Papers I** and **II**, and what is presented here is a very short overview. For convenience, the experimental setup is repeated here [see Fig. 5.3(a)]. The system contains a vector network analyzer (VNA), which is contained in a metallic box, and a set of four antennas which are attached to the metallic box. The box is mounted on a 3 m long rail that is supported by two poles. The total weight of the box is about 30 kg, and for a better stability, the poles are fitted into a tripod. The operation of the system is controlled by a laptop computer and all non-manual operations are powered by a generator.

Aperture synthesis in azimuth is achieved by displacing the system along

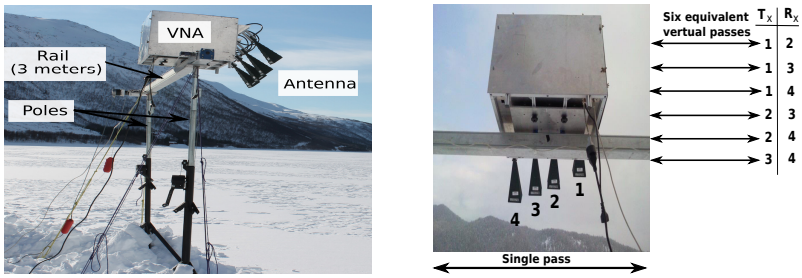

(a) (b)

(c) (d)

Figure 5.3: The set up and aperture synthesis of the TomoSAR system. (a) The set up of the GB-SAR system; (b) Demonstration of aperture synthesis in the vertical direction by utilizing a multistatic radar system. T_x and R_x refer to the transmitting and receiving channels, respectively. (c) The array of 4 antennas can be manually moved up and down along the VNA box to increase the length of the vertical aperture. (d) The rail can be manually moved up and down along the poles to further increase the number of acquisitions.

the rail using a stepper motor. Consequently, the acquisition positions are known precisely for accurate azimuth focusing. However, aperture synthesis in the elevation is achieved in a different manner, i.e., by forming an antenna array from the four horn antennas which are displaced in the vertical direction. Each of the four antennas can be operated as a transmitter or receiver and form a multistatic configuration. In a single pass, six acquisitions can be obtained from the different combinations of the four antennas. Fig 5.3(b) shows the different transmit-receive combinations of the four antennas in producing

six virtual parallel passes from a single pass. As it is discussed in chapter 4, the vertical resolution can be improved by having as many parallel passes as possible. The poSAR system achieves this by operating in a repeat pass mode. This is done in two ways. The first is by manually moving the set of the four antennas up and down along the VNA box [see Fig 5.3(c)], and the second, is also by manually moving the rail up and down along the poles [see Fig 5.3(d)]. The revisit time between two consecutive passes may vary from 10 to 20 minutes. Due to the manual operations involved in achieving multiple passes, the relative position between any two different passes is in general not known to within a sub-wavelength accuracy. Therefore, a calibration procedure is required to estimate the vertical positions of the sensors directly from the data.

The PoSAR system can operate at different frequency bands, including C, X, and Ku-bands, and over different polarization channels. The system is a very high resolution system. For example, at X-band, resolution values of 3.75 cm in ground range, 1.73 cm in azimuth and 6 cm (for 36 acquisitions) in elevation can be achieved. Typical scene dimensions that can be imaged using the system are 6 and 8 meters in azimuth and ground range directions, respectively.

5.1.3 Datasets

The TomoSAR experimental datasets used in this thesis are collected at X-, and C-band with center frequencies of 10 and 5.845 GHz, respectively; and bandwidths of 4 and 2.41 GHz respectively. The datasets also include measurements acquired at two polarizations, VV and HV. Most of the results presented in **papers I** and **II** are based on 36 acquisitions, which are obtained from 6 passes. Table 5.2 summarises the tomographic datasets used in the papers.

Table 5.2: Tomographic datasets used in **Papers I** and **II**.

Test sites	**# of acquisitions**	**Polarization**	**Frequency**	**Used in**
Kattfjord	36	VV	X-	**Papers I** and **II**
	15	VV	X-	**Paper I**
	15	HV	X-	**Paper I**
Prestvannet lake	36	VV	X-	**Paper II**
	36	VV	C-	**Paper II**

5.2 Spaceborne InSAR, helicopter-borne laser and stereo camera acquisitions

The second part of the work in this thesis, which deals with sea ice topographic height retrieval using across-track InSAR, is based on datasets collected during a Fram Strait cruise campaign lead by the Norwegian Polar Institute during the late summer of 2016. During the campaign, a coordinated collection of Satellite InSAR and helicopter-borne measurements was performed

5.2.1 Study area

The datasets were collected in the Fram Strait located between Greenland and Svalbard in the Arctic. The sea ice in the Fram Strait is very dynamic owing to the transport of ice by the transpolar drift [Renner et al., 2014]. Consequently, both first year and multiyear ice with various degrees of deformation exist in the region. The study in this thesis focuses on a landfast ice region, which consists of grounded multiyear sea ice. The mean thickness of the sea ice was about 3 m, with a maximum of 8 to $10\ m$ in some parts. The area of interest consists of sea ice ridges as high as 2 to 3 meters. From field observations, it is known that the sea ice surface in the vicinity of the investigated transect is snow free. The map of the area is shown in Fig. 5.4

5.2.2 TanDEM-X InSAR data sets

The interferometric dataset considered in this study is acquired by TanDEM-X in the alternating bistatic acquisition mode [Krieger et al., 2007]. The two images that form the InSAR pair are acquired at VV polarization, with an incidence angle of $39.7\,^{\circ}$, having a spatial resolution of $3.3m \times 1.84m$ in azimuth and ground range, respectively. Table 5.3 lists some of the parameters of the InSAR acquisition.

5.2.3 Helicopter-borne in situ measurements

During the same day, spatially overlapping helicopter surveys were conducted to collect additional complementary data. The helicopter was equipped with two main instruments, an EM-bird [Haas et al., 2009] and a stereo camera [Divine et al., 2016].

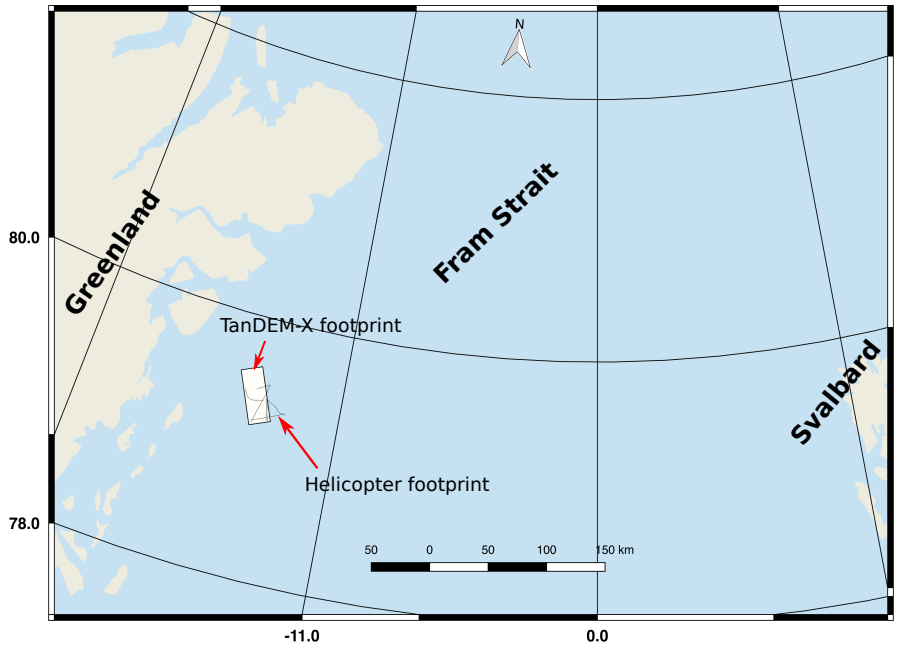

Figure 5.4: Map of Fram Strait test site and footprints of the satellite and helicopter acquisitions.

Table 5.3: Some parameters of the TanDEM-X acquisition.

Attributes	**Values**
Polarization	VV
Incidence angle	39.7 °
Perpendicular baseline	411.64m
Mode	Alternating bistatic

Laser Altimeter and EM induction sounder

The EM-bird, which is towed underneath the helicopter, consists of two instruments, a laser profiler and an EM induction sounder. The former is used to derive sea ice surface topography and the combination of the two is used to

estimate sea ice thickness [Haas et al., 2009]. Fig. 5.5(a) shows the EM-bird instrument. The altitude of the EM-bird above the surface varies between 10 and 15 m. For this altitude, the footprint of the laser is about 0.1 m, whereas the foot print of the EM induction sounder is about 50 m. The laser is capable of measuring distance with an accuracy of ± 15 mm. On the other hand, the derived sea ice thickness has an accuracy of $\pm 0.1m$ over level ice, however, due to the larger footprint of the induction sounder, the thickness of highly deformed sea ice structures such as big ridges can be underestimated [Haas et al., 2009], [Renner et al., 2014]. The derived sea ice surface profile from the laser data is composed of two components: a high frequency component representing the surface height variations and a low frequency component caused by altitude and attitude variations of the helicopter. The latter is removed by applying a three-step filtering process proposed in [Hibler, 1972].

ICE stereo camera

Another instrument on the helicopter, which is used to acquire information about the sea ice surface topography was the ICE stereo camera [Divine et al., 2016]. The stereo camera system is contained in an aerodynamic inclosure which is attached to the underside of the helicopter, at the front [see Fig. 5.5(b)]. The sea ice surface topography is derived from the stereo camera data using photogrammetric techniques [Divine et al., 2016]. During data collection, the footprint of the stereo camera system varied between 40 and 60 m. Therefore, unlike the laser altimeter, which is a point measurement, the profile obtained from the stereo camera covers a swath width varying between 40 and 60 m. Using this technique, it is reported that the the small-scale height variations of the sea ice surface can be reconstructed with a Root-Mean-Square-Error of about 4 cm [Divine et al., 2016].

5.3 Challenges and limitations

Even though ground-based measurements are crucial for validating remote sensing measurements from airborne and spaceborne acquisitions, as well as making detailed analysis at a very fine scale, there are some challenges associated with data collection over snow and ice. Sea ice in particular is a dynamic medium and it is always a challenge to deploy ground-based instruments. Tomographic SAR data collection using the ground-based SAR system introduced above requires many manual operations such as transporting the

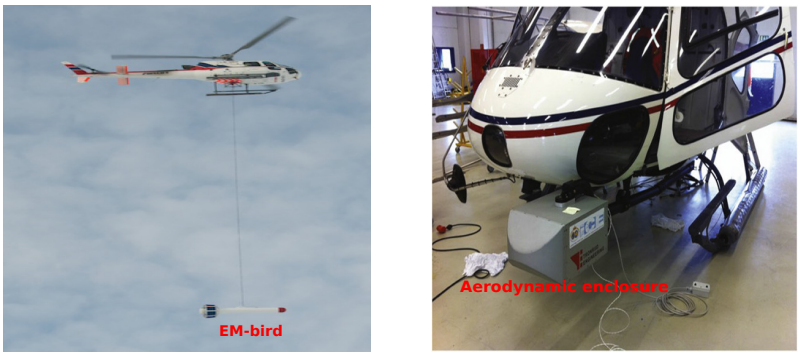

(a) (b)

Figure 5.5: Helicopter-borne instruments. (a) EM-bird towed beneath the helicopter [Fors, 2017], and (b) Aerodynamic enclosure of ICE stereocamera system [Divine et al., 2016].

equipments by walking over the ice, installing the radar system and moving the system up and down along the supports to increase the number of parallel acquisitions. These tasks require staying on the ice for many hours. Therefore, it is important to make sure that the ice is stable enough to support the loads of the equipment and personnel. Consequently, our study has been limited to a stable, immobile, and low-saline fjord and lake ice. Moreover, it is impractical to install the system on vey tall vertical supports, and consequently the observed scene has been limited to a few meters in azimuth and range directions.

Modelling the radar backscatter of snow and ice requires precise quantitative description of the physical state of the medium. For example, the backscatter contributions of the surface and interface features can be modelled through accurate knowledge of the small scale roughness of the surfaces. However, for the snow-ice interface in particular, surface roughness measurements can only be made after manually removing the snow cover from the ice, a process which can not be achieved without destructing the actual surface roughness structures. For modelling the ice volume backscatter contributions, statistical descriptions of the ice volume can be obtained from thin and thick ice core sections processed on special ice laboratories. Due to some technical issues, such detailed microstructure of the snow and ice samples has not been analyzed,

and therefore modelling of the actual radar backscatter has not be considered in this thesis.

Coordinating satellite data acquisition with helicopter in situ measurements is also a challenge as it requires some planning and good luck with respect to weather conditions for flying the helicopter. During the TanDEM-X data acquisition, the helicopter flights were conducted about 7 - 8 hours prior to the satellite acquisitions. Consequently, even though the satellite scenes contain both slowly drifting and fast ice, our analysis has been limited to the stable fast ice region. Moreover, the helicopter did not land on the ice, and the closest the EM-bird instrument got to the surface was about 15 meters. Therefore, all the laser and photogrammetric validation data in **Paper III** refer to quantities estimated from measurements made from the helicopter.

Chapter 6

Brief overview of Publications

This chapter gives an overview of the scientific contributions of the work in this thesis. It summarizes the three journal papers which make up the main body of the thesis, and lists conference paper contributions at the end.

6.1 Summarizing Journal publications

Paper I

T. G. Yitayew, L. Ferro-Famil, T. Eltoft, and S. Tebaldini, "**Tomographic imaging of fjord ice using a very high resolution ground-based SAR system**," *IEEE Transactions on Geoscience and Remote Sensing*, vol. 55, no. 2, pp. 698-714, 2017.

Characterisation of the vertical layering structure and analysis of the local distribution of the scatterers in snow and ice requires the use of imaging techniques allowing for a description of these complex volumetric media in a 3D space. The paper presents experimental results involving tomographic imaging of a snow covered fjord ice using the ground based SAR system introduced in chapter 5. The collected TomoSAR datasets and the test site, which contains a snow covered seasonal fjord ice from Kattfjord, Tromsø, Norway are already introduced in chapter 5. The thickness of the snow cover at the test site was about $24\ cm$, where as the thickness of the ice layer was about $28\ cm$. Very

interesting and new results on imaging the vertical structure of the radar reflectivity of the medium, and snow and ice parameter estimation are presented in the study.

The distribution of the radar reflectivity of the investigated snow and ice layers is presented in the form of tomograms which are 2D vertical sections of the 3D focussed image. The time domain backprojection algorithm is used for tomographic SAR focusing. The tomograms reveal important information such as the vertical position of the dominant contributions in the snow-ice-water complex medium - information that can not be accessed through the conventional 2D SAR imaging technique. Moreover, the tomograms are used to investigate the effect of changes in the propagation velocity of the radar waves inside the snow and ice layers on the focusing process. It is found that the information from the tomograms is "distorted" as a result of not properly taking into account the changes in propagation velocity and refraction during the focusing process. The distortion by itself is found to be useful to estimate the refractive indices of the snow and ice layers which are eventually used to correct the distorted tomograms by means of a post-focusing correction procedure. A refractive index value of $1.4 \pm 17\%$ for the snow layer and $1.7 \pm 20\%$ for the ice layer are estimated. These estimated values are compared with values reported in the literature, and good agreement has been found.

The analysis is supported by conducting a simulation experiment to synthesize the setup of the tomographic SAR system used for data collection. The distortion of the tomographic information and the angular radiation pattern at the interfaces are successfully simulated by taking into account the changes in propagation velocity and refraction effects during the raw SAR data generation, by using a scattering model assuming ideal small scale roughness at the interfaces and ideal point scatterers in the volume.

The contributions of the different scattering components in the snow and ice layers are also investigated. The small scale roughness at the interfaces between the air-snow-ice-water complex medium, the change in dielectric properties across the interfaces, the formation of a snow crust at the top surface of the snow layer, the degree of homogeneity and dryness of the snow volume, the abundance of air bubbles in the ice layer are found to be most influential in determining the relative strength of the radar reflectivity in the vertical direction.

To demonstrate the practical applicabilities of the information presented in the tomograms, the radar reflectivity of the complex medium is presented by plotting the scattering contribution of the different parts of the considered medium as a function of depth and incidence angle. It is discussed that such

plots can be useful to validate and interpret measurements acquired by other 2D SAR sensors operating at the same sensor parameters. Moreover, the applicability of such information for snow and ice radar backscatter modelling is discussed, as such plots reveal the location of the dominant scattering contributions and the preponderant scattering mechanisms inside the semi-transparent volume.

The vertical structure of the radar reflectivity of the investigated medium is imaged and compared at two polarizations, VV and HV. The results from comparing VV and HV measurements reveal that, even though the response at HV is weaker than the corresponding response at VV, most of the HV responses are associated to the ice and the ice-seawater interfaces.

Paper II

T. G. Yitayew, L. Ferro-Famil, T. Eltoft, and S. Tebaldini, "**Lake and fjord ice imaging using a multifrequency ground-based tomographic SAR system**," *IEEE Journal of Selected Topics in Applied Earth Observations and Remote Sensing*, vol. PP, no. 99, pp. 1-12, 2017.

As a continuation of our investigation of a snow covered ice medium using SAR tomography, we extended the analysis and interpretation of **Paper I** by including more datasets collected over snow covered lake ice in a multifrequency setup of the same system introduced in chapter 5. In addition to extending the techniques presented in **paper I**, this study aimed at comparing the snow covered fjord ice and lake ice in terms of their vertical stratification and estimated parameters. Moreover, the study investigated the response of the lake ice medium at two different frequencies, X-, and C-band. The lake ice data were collected at Prestvannet frozen lake, located in Tromsø, Norway. The thickness of the snow cover was about $20\ cm$, whereas the thickness of the lake ice layer was about $90\ cm$.

The joint analysis of the X-band tomograms of the fjord ice and lake ice datasets reveal that the backscatter contribution at the interfaces is stronger than the response from the section of the layers in between the interfaces. This analysis further consolidates the statements made in **paper I** regarding the contributions of the small scale roughness at the interfaces, the dielectric contrast between adjacent layers and the air bubbles to the relatively strong backscatter signal at and around the interfaces. Many of the similarities and differences

in physical properties of the investigated media, such as inhomogeneity and depths of the snow and ice layers, between the two test sites are easily captured by the high resolution tomographic acquisition system.

The distortion of the tomograms, which was investigated in **paper I**, is also apparent in the lake ice tomograms. However, multiple sub-layers were detected in the lake ice layer. The formulation presented in **paper I** for modelling the distortion of the different layers in the tomograms was only for two layers, and due to the presence of more than two layers in the lake ice data, the formulation had to be extended. Consequently, we presented a mathematical derivation which describes electromagnetic wave propagation across a multilayer medium, and introduced a simple optimization scheme for estimating the depth and refractive indices of a multilayer medium with arbitrary but finite number of layers. Refractive index values of $1.3 \pm 6\%$ for the snow layers on top of the lake ice, $1.53 \pm 11\%$, and $1.74 \pm 20\%$ for two ice sub-layers are found. The estimated refractive indices and the depths of the snow and ice layers for both datasets are validated by comparing the estimated depths with measured values. A good agreement has been found.

The 3D response of the snow covered lake ice medium is investigated and compared at two frequencies, X-, and C-band. It is found that the volume contributions of the snow and ice layers are very weak at C-band compared to that of X-band. Moreover, the C-band backscatter of the interfaces is dominated by near nadir response compared to that of X-band. These two observations are associated to the difference in wavelength compared to the scale of the scattering elements (snow grains in the snow layer and air bubbles in the lake ice layer), and the angular radiation pattern of monostatic radar antennas, respectively.

Paper III

T. G. Yitayew, D. V. Divine, W. Dierking, T. Eltoft, L. Ferro-Famil, A. Rosel, and J. Negrel, "**Validation of Sea ice Topographic Heights Derived from TanDEM-X Interferometric SAR Data with Results from Laser Profiler and Photogrammetry**," *IEEE Transactions on Geoscience and Remote Sensing*, pp. 1-17;, 2017.

The second part of the work in this thesis is presented in this paper. The surface topography of sea ice is an important parameter for a number of applications such as climate studies and sea ice parameter retrieval. In this paper the technique of SAR interferometry is investigated for estimating the local topography of the sea ice surface. TanDEM-X interferometric datasets that are acquired over the Fram Strait region in the Arctic, located between Greenland and Svalbard, are used. The area of interest contains grounded multiyear fast ice. The analysis focuses on an 8 km segment, where independent helicopter-borne stereo camera and laser altimeter *in situ* measurements are also available from overlapping flights.

The local topography of the sea ice surface is derived from the stereocamera data using photogrammetric techniques, whereas advanced filtering techniques are employed for the laser altimeter data. Then, the local topography of sea ice retrieved from TanDEM-X is compared with the one derived from the two *in situ* measurements. For a proper comparison, the three datasets are made compatible by an extensive preprocessing. However, it is noted that the laser altimeter data is a point measurement and consequently equivalent averaging with respect to the across-track direction of the helicopter flight was not possible. On the other hand, the stereocamera data has a swath width of about 40 to 60 m and has been processed using the same window size as the TanDEM-X data. The root-mean-squared-error and ridge statistics such as the number of detected ridges, the average and the maximum height of ridges are used for comparison.

The comparison of the retrieved sea ice topographic height values from the TanDEM-X acquisitions with those derived from the stereocamera measurements reveal that 80% of the ridges with height values greater than 0.5 m can be estimated with a root-mean-squared-error value which is less than or equal to 0.3 m, with the relative error decreasing significantly as a function of ridge height. Moreover, the applicability of the topographic height information derived from the laser altimeter data for validating the corresponding values from TanDEM-X is investigated. For bigger sea ice ridges (with respect to the

multilook window size used for processing the InSAR data), it is found that the topographic information derived from one-dimensional laser altimeter data can be well used to validate the TanDEM-X height maps. The need for multilook averaging to reduce the phase noise is identified as the main challenge in retrieving the sea ice surface topographic information using SAR interferometry.

6.2 List of other contributions

1. T. G. Yitayew, L. Ferro-Famil, and T. Eltoft, "High resolution three-dimensional imaging of sea ice using ground-based tomographic SAR data," in EUSAR 2014; *10th European Conference on Synthetic Aperture Radar*; Proceedings of. VDE, 2014, pp. 1-4.

2. T. G. Yitayew, L. Ferro-Famil, and T. Eltoft, "3-D imaging of sea ice using ground-based tomographic SAR data and comparison of the measurements with TerraSAR-X data," in *Geoscience and Remote Sensing Symposium (IGARSS), 2014 IEEE International*. IEEE, 2014, pp. 1329-1332.

3. T. G. Yitayew, L. Ferro-Famil et al., "Investigation of sea ice and lake ice using ground-based SAR tomography," in *2015 IEEE International Geoscience and Remote Sensing Symposium (IGARSS)*. IEEE, 2015, pp. 5276-5279.

4. T. G. Yitayew, A. P. Doulgeris, T. Eltoft, W. Dierking, C. Brekke, and A. a. Rosel, "Sea ice segmentation using TanDEM-X pursuit monostatic and alternating bistatic modes," in *2017 IEEE International Geoscience and Remote Sensing Symposium (IGARSS)*. IEEE, 2017.

Chapter 7

Paper I:
Tomographic imaging of fjord ice using a very high resolution ground-based SAR system

T. G. Yitayew, L. Ferro-Famil, T. Eltoft, and S. Tebaldini
Published in: *IEEE Transactions on Geoscience and Remote Sensing*, vol. 55, no. 2, pp. 698-714, 2017.

Chapter 8

Paper II:
Lake and fjord ice imaging using a multifrequency ground-based tomographic SAR system

T. G. Yitayew, L. Ferro-Famil, T. Eltoft, and S. Tebaldini

Published in: *IEEE Journal of Selected Topics in Applied Earth Observations and Remote Sensing*, vol. 10, no. 10, pp. 4457 - 4468, 2017.

Chapter 9

Paper III:
Validation of sea ice topographic heights derived from TanDEM-X interferometric SAR data with results from laser profiler and photogrammetry

T. G. Yitayew, W. Dierking, D. V. Divine, T. Eltoft, L. Ferro-Famil, A. Rosel, and J. Negrel,

Submitted to: *IEEE Transactions on Geoscience and Remote Sensing*, on 11^{th} of September 2017

Chapter 10

Conclusion and outlook

This chapter provides concluding remarks and suggestions for future research.

10.1 Conclusion

In this thesis, imaging of different types of ice in the vertical direction is investigated by using the techniques of SAR tomography and across-track interferometry. The study shows the capability of the two techniques when it comes to imaging the vertical scattering distribution of snow and ice volumes and topographic height retrieval of sea ice, respectively.

In **Papers I** and **II**, a very high resolution ground-based SAR system operated at multiple frequencies and polarizations is used for tomographic imaging of fjord and lake ice. In both cases, the test sites contain snow covered seasonal ice. The fjord ice was less silane than ordinary sea ice. The thicknesses of the snow and ice layers were a few tens of centimeters. The distributions of the radar reflectivity of the investigated snow and ice layers are presented in the form of tomograms, which are 2D vertical sections of the 3D focussed image.

The contributions of the different scattering components in the snow and ice media are investigated in **Papers I** and **II**. In both the fjord and lake ice cases, the backscatter signal at the interfaces is found to be stronger than the response from the volume between the interfaces. This is explained by the scattering being associated to the small scale roughness at the interfaces between the air-snow, snow-ice, and ice-water, and the dielectric contrast across the interfaces. The strength of the scattering contributions of the snow and ice

volumes is also investigated and compared at both test sites. For most of the volume investigated at X-band, the backscatter contribution from the ice volume is found to be superior to the corresponding snow volume contribution. This is attributed to the abundance of the air bubbles which are irregularly shaped and randomly oriented throughout most of the ice volume. The results also reveal that X-band backscatter from a dry and homogeneous snow layer is not negligible. Moreover, it is found that the formation of snow crusts at the top of the snow layer increases the snow backscatter. Therefore, in a snow-ice-water complex medium, the backscatter response is a cumulative effect of the small scale roughness of the interfaces between the different layers of snow and ice, and the dielectric discontinuity caused by the volume inhomogeneities inside the snow and ice, with the contribution of the ice layer being much higher than that of the snow.

The physics of wave propagation inside the snow-ice-water complex medium is also investigated in **Papers I** and **II**. It is found that the tomograms are distorted as a result of not properly taking into account the change in propagation velocity and refraction during the focusing process. Therefore, for proper interpretation of the tomograms, it is highlighted that the refraction phenomenon should be taken into account during tomographic focusing. Moreover, the transmitted wave experiences a change in wavelength and local incidence angle while it propagates across the interfaces. These phenomena have been taken into account during the analysis of the scattering process at the lower layers. The distortion of the tomograms is found to be useful to estimate the depth and the refractive indices of the snow and ice layers, and eventually correct the tomograms by means of a post-focusing correction procedure. First, a rigorous mathematical formulation which describes wave propagation across a dense multilayer medium is presented, and then, based on the formulation, an optimization scheme is presented for estimating the depth and the refractive indices of a multilayer medium with finite number of layers. The estimation procedure is demonstrated on the lake ice data set with three layers, and the fjord ice data set with two layers. The estimated depth and refractive indices of the snow and ice layers are validated by applying a correction procedure on the distorted tomograms and comparing the position of the layers against *in situ* measurements. A good agreement between the measured and retrieved depth positions of the snow and ice layers is found.

The practical applicability of the information from the tomograms is also discussed throughout the two papers. The information improves our understanding of the nature of interactions of radar waves with snow and ice. The presented results may divulge useful information for EM scattering modellers

as they reveal the magnitude and the specific vertical positions of the dominant scattering mechanism. Moreover, simple plots extracted from the tomograms can be used to compare and validate measurements acquired by other conventional airborne and spaceborne SAR sensors operating at the same parameters.

The surface and volume responses of the snow covered fjord ice at two polarizations, VV and HV, are also investigated and compared in **Paper I**. The results reveal that the HV response of the ice layer is remarkably stronger than that of the snow layer. This is associated to the depolarizing capability of irregularly shaped and randomly oriented air bubbles in the ice layer. It is also observed that the VV response of the observed medium is stronger than the corresponding response at HV.

In **Paper II**, the vertical structure of the reflectivity of the snow covered lake ice is investigated and compared at two frequencies X-, and C-band. The volume contributions of the snow and ice layers are very weak at C-band compared to that of X-band. Moreover, the response at the interfaces at C-band is limited to the small incidence angle values compared to that of X-band. This is explained to be attributed to the difference in the wavelengths with respect to the scale of surface and volume scattering features.

In summary, the work in **Papers I** and **II** shows the great potential of SAR tomography for identifying the vertical position of the dominant scattering centers and the dominant scattering mechanisms in snow and ice, retrieving information such as the refractive indices and depths of the multiple layers of snow and ice that can not be accessed through 2D SAR imaging, and studying and comparing the responses of snow and ice volumes to different radar frequencies and polarizations. Through the presented results, a significant contribution towards an improved understanding of the interaction of microwaves at the two frequencies X-, and C-band, and the two polarizations VV and HV with the snow-ice-water complex medium is achieved.

In **paper III**, the local topography of the sea ice surface is investigated using an interferometric SAR data set acquired by TanDEM-X. The retrieved InSAR heights over an 8 km segment are compared with helicopter-borne stereo camera and laser profiler measurements acquired the same day. It is found that 80% of the ridges with height values greater than 0.5 m can be estimated with an RMSE less than or equal to 0.3 m, with the relative error decreasing significantly as a function of ridge height. The results also show that the topographic information derived from one-dimensional laser altimeter profiles can be well used to validate the TanDEM-X height maps when the width of the ice surface structures is comparable or larger than the size of the averaging window used for interferometric processing. Sea ice ridge statistics such as the number

of detected ridges, the maximum, minimum, and average heights of the individual ridges are found to provide complementary information and to support the comparison of the different measurement devices. The need for multilook averaging to reduce the phase noise causes loss of vertical resolution and is identified as the main challenge when it comes to the use of InSAR for sea ice topographic retrieval.

10.2 Outlook

Tomographic SAR imaging using 2D synthetic arrays has been applied mainly for forest, urban, and glacier scenarios since its introduction in the year 2000. However, its application to sea ice is limited mainly due to the dynamic nature of the ice. In general, the surface and volumetric properties of the ice changes within a relatively short period of time. Moreover, sea ice can be in constant drift in response to wind, ocean currents and tidal forces. Therefore, the multibaseline measurements required for tomographic imaging of ice in general need to be collected over a very short duration. In our tomographic experiments, the temporal separation between two passes, where each pass corresponds to six measurements, varied between 10 and 20 minutes. Consequently temporal decorrelation was not an issue. However, the experiments were conducted over an immobile low-saline fjord and and lake ice. Similar experiments are encouraged to further investigate different aspects of multibaseline imaging of sea ice and extend the validity range of the results presented here.

The ground-based tomographic SAR system was operated from a very low altitude. Moreover, the system was installed on a fixed 3 m rail. Consequently, the presented results correspond to a small patch of ground. Therefore, for large scale imaging and monitoring of sea ice, the acquisition has to be performed from higher altitudes with aircrafts and satellites. The spaceborne platforms are best when it comes to spatial coverage and stability. However, in practice, such a configuration requires very complex systems or many satellites flying in close formation. That could be rialized in the future, however, at the moment no such systems are available. A repeat-pass mode, for example, multi-pass TanDEM-X acquisitions, could be used, however, temporal decorrelation is an issue for sea ice in particular. The more realistic option at the moment is using airborne platforms. Therefore, a similar experiment over ordinary sea ice can be conducted by SAR systems onboard aircrafts. However, a number of issues need to be considered. Airborne multibaseline acquisitions using a single SAR system can only be achieved by repeatedly flying over a

given area of interest, which requires a certain period of time. Therefore, such techniques are still limited to a relatively stable ice as one has to make sure that the changes in the ice properties, such as the position and internal structures of the scattering centers, do not exceed the size of the resolution cells. If the drift of the ice is significant, repeat-pass mode airborne SAR tomography will not give reliable results. In those cases, the most probable option would be to deduce high resolution volumetric information such as the thickness of sea ice via the surface topographic information which in turn can be retrieved from single-pass InSAR systems onboard satellites and aircrafts.

Another issue associated to multibaseline acquisitions is the challenge of achieving perfectly parallel tracks. In our tomographic experiment the multistatic acquisition system was mounted on a rigid 3 m long rail. Even though the relative elevation position between any two passes was not known to a fraction of the wavelength, the multibaseline acquisitions by default were parallel to each other. However, for airborne acquisitions maintaining perfectly parallel flight paths is a challenge. Consequently, the data are susceptible to phase errors associated to turbulence and uncertainty of their positioning systems. Therefore, before tomographic image focusing, preprocessing steps such as motion compensation and phase calibration are required.

As it is extensively discussed in this thesis, time domain backprojection is an ideal focusing approach for tomographic SAR data over volumetric media. However, it is computationally inefficient. Therefore, adaption to the backprojection focusing needs to be made as the size of airborne SAR images are in general bigger than the size of the images considered in this study. Parallel computing or other approximations can be explored to make it faster. Another issue that has to be considered in airborne SAR imaging is realtime processing. To detect any possible problems associated to the SAR imaging process during the flight, realtime processing is vital. Frequency domain focusing techniques can be used to produce quicklook SAR images with lower resolution.

As it is discussed in the thesis, the whole concept of snow and ice 3D reconstruction using SAR tomography is based on a reasonable amount of penetration, i.e., in the order of many wavelengths. The penetration depth into the snow and ice layers depends on many factors such as the wetness and homogeneity of the snow cover, the temperature and salinity of the ice volume, and the operating wavelength of the radar system. Therefore, tomographic data collection campaigns over snow and ice should take into account these factors. Microwave frequencies such as X-, and C-band can only penetrate a few centimeters into first year ice, where as longer wavelengths such as P-band can have a penetration depth of 1 to 1.5 meters. Therefore, tomographic SAR analysis of

first year sea ice can only be done for the top few centimeters and meters of layers. In relation to the issue of penetration, our results from the lake ice experiment reveal that both X-, and C-band well penetrate into fresh water ice. This implies that both frequencies can penetrate into the upper part of glaciers. Theoretical studies show that a minimum penetration depth of about 10 m and 30 m can be achieved under dry conditions at X-, and C-band, respectively. Therefore, airborne tomographic experiments over glaciers using these frequency bands will be an interesting subject, as such results can be used to validate the use of SAR data from the current spaceborne SAR systems such as TerrSAR-X and Sentinel-1 satellites.

Finally, it is interesting to note that the retrieval of the mean surface topography of sea ice using across-track interferometry is optimal when the penetration depth is negligible. However, as is just discussed, microwave frequencies do penetrate into the ice to some degree, and consequently, there is an associated loss of coherence. The presence of open water, melt ponds, open and refrozen leads also causes loss of coherence. These are the challenges one has to face when it comes to the use of the InSAR technique for sea ice applications.

Bibliography

[Aldenhoff et al., 2016] Aldenhoff, W., Berg, A., and Eriksson, L. E. (2016). Sea ice concentration estimation from Sentinel-1 synthetic aperture radar images over the Fram Strait. In *Geoscience and Remote Sensing Symposium (IGARSS), 2016 IEEE International*, pages 7675–7677. IEEE.

[Amelung et al., 1999] Amelung, F., Galloway, D. L., Bell, J. W., Zebker, H. A., and Laczniak, R. J. (1999). Sensing the ups and downs of Las Vegas: InSAR reveals structural control of land subsidence and aquifer-system deformation. *Geology*, 27(6):483–486.

[Bamler and Hartl, 1998] Bamler, R. and Hartl, P. (1998). Synthetic aperture radar interferometry. *Inverse problems*, 14(4):R1.

[Banda et al., 2016] Banda, F., Dall, J., and Tebaldini, S. (2016). Single and multipolarimetric P-band SAR tomography of subsurface ice structure. *IEEE Transactions on Geoscience and Remote Sensing*, 54(5):2832–2845.

[Barber et al., 1992] Barber, D. G., LeDrew, E. F., Flett, D., Shokr, M., and Falkingham, J. (1992). Seasonal and diurnal variations in SAR signatures of landfast sea ice. *IEEE transactions on geoscience and remote sensing*, 30(3):638–642.

[Berg et al., 2015] Berg, A., Dammert, P., and Eriksson, L. E. (2015). X-band interferometric SAR observations of Baltic fast ice. *IEEE Transactions on Geoscience and Remote Sensing*, 53(3):1248–1256.

[Birkeland, 1998] Birkeland, K. W. (1998). Terminology and predominant processes associated with the formation of weak layers of near-surface faceted crystals in the mountain snowpack. *Arctic and Alpine Research*, pages 193–199.

[Cafforio et al., 1991] Cafforio, C., Prati, C., and Rocca, F. (1991). SAR data focusing using seismic migration techniques. *IEEE transactions on aerospace and electronic systems*, 27(2):194–207.

[Cantalloube and Dubois-Fernandez, 2006] Cantalloube, H. and Dubois-Fernandez, P. (2006). Airborne X-band SAR imaging with 10 cm resolution: Technical challenge and preliminary results. *IEE Proceedings-Radar, Sonar and Navigation*, 153(2):163–176.

[Carsey, 1992] Carsey, F. D. (1992). *Microwave remote sensing of sea ice*. American Geophysical Union.

[Cloude, 2009] Cloude, S. (2009). *Polarisation: applications in remote sensing*. Oxford University Press.

[Cloude and Papathanassiou, 2003] Cloude, S. and Papathanassiou, K. (2003). Three-stage inversion process for polarimetric SAR interferometry. *IEE Proceedings-Radar, Sonar and Navigation*, 150(3):125–134.

[Cloude and Papathanassiou, 1998] Cloude, S. R. and Papathanassiou, K. P. (1998). Polarimetric SAR interferometry. *IEEE Transactions on Geoscience and Remote Sensing*, 36(5):1551–1565.

[Crocker, 1992] Crocker, G. (1992). Observations of the snowcover on sea ice in the Gulf of Bothnia. *International Journal of Remote Sensing*, 13(13):2433–2445.

[Cumming and Wong, 2005] Cumming, I. G. and Wong, F. H. (2005). *Digital processing of synthetic aperture radar data: algorithms and implementation*. Artech House.

[Curlander and McDonough, 1991] Curlander, J. C. and McDonough, R. N. (1991). *Synthetic aperture radar*. John Wiley & Sons New York, NY, USA.

[Dierking et al., 2017] Dierking, W., Lang, O., and Busche, T. (2017). Sea ice local surface topography from single-pass satellite InSAR measurements: a feasibility study. *The Cryosphere*, doi:105194/tc-2017-40, 2017. Under review.

[Divine et al., 2016] Divine, D. V., Pedersen, C. A., Karlsen, T. I., Aas, H. F., Granskog, M. A., Hudson, S. R., and Gerland, S. (2016). Photogrammetric retrieval and analysis of small scale sea ice topography during summer melt. *Cold Regions Science and Technology*, 129:77–84.

[Ferretti et al., 1999] Ferretti, A., Prati, C., and Rocca, F. (1999). Multibaseline InSAR DEM reconstruction: The wavelet approach. *IEEE Transactions on Geoscience and Remote Sensing*, 37(2):705–715.

[Ferretti et al., 2001] Ferretti, A., Prati, C., and Rocca, F. (2001). Permanent scatterers in SAR interferometry. *IEEE Transactions on geoscience and remote sensing*, 39(1):8–20.

[Ferro-Famil et al., 2015] Ferro-Famil, L., Huang, Y., and Pottier, E. (2015). Principles and applications of polarimetric SAR tomography for the characterization of complex environments. In *VIII Hotine-Marussi Symposium on Mathematical Geodesy*, pages 243–255. Springer.

[Fornaro et al., 2014] Fornaro, G., Lombardini, F., Pauciullo, A., Reale, D., and Viviani, F. (2014). Tomographic processing of interferometric SAR data: Developments, applications, and future research perspectives. *IEEE Signal Processing Magazine*, 31(4):41–50.

[Fornaro et al., 2012] Fornaro, G., Reale, D., Pauciullo, A., Zhu, X. X., and Bamler, R. (2012). SAR tomography: an advanced tool for spaceborne 4D radar scanning with application to imaging and monitoring of cities and single buildings. *IEEE Geoscience and Remote Sensing Newsletter*, pages 9–17.

[Fornaro et al., 2010] Fornaro, G., Serafino, F., and Reale, D. (2010). 4-D SAR imaging: The case study of rome. *IEEE Geoscience and Remote Sensing Letters*, 7(2):236–240.

[Fornaro et al., 2003] Fornaro, G., Serafino, F., and Soldovieri, F. (2003). Three-dimensional focusing with multipass SAR data. *IEEE Transactions on Geoscience and Remote Sensing*, 41(3):507–517.

[Fors, 2017] Fors, A. S. (2017). *Investigation of summer sea ice with X and C-band multi-polarimetric synthetic aperture radar*. PhD thesis, UIT The Arctic University of Norway.

[Franceschetti and Lanari, 1999] Franceschetti, G. and Lanari, R. (1999). *Synthetic aperture radar processing*. CRC press.

[Frey, 2010] Frey, O. (2010). *Synthetic aperture radar imaging in the time domain for nonlinear sensor trajectories and SAR tomography*. PhD thesis, University of Zurich.

[Fung, 1994] Fung, A. K. (1994). *Microwave scattering and emission models and their applications*. Artech house.

[Gabriel et al., 1989] Gabriel, A. K., Goldstein, R. M., and Zebker, H. A. (1989). Mapping small elevation changes over large areas: differential radar interferometry. *Journal of Geophysical Research: Solid Earth*, 94(B7):9183–9191.

[Garbrecht et al., 2002] Garbrecht, T., Lüpkes, C., Hartmann, J., and Wolff, M. (2002). Atmospheric drag coefficients over sea ice—validation of a parameterisation concept. *Tellus A*, 54(2):205–219.

[Gini and Lombardini, 2005] Gini, F. and Lombardini, F. (2005). Multibaseline cross-track SAR interferometry: A signal processing perspective. *IEEE Aerospace and Electronic Systems Magazine*, 20(8):71–93.

[Gini et al., 2002] Gini, F., Lombardini, F., and Montanari, M. (2002). Layover solution in multibaseline SAR interferometry. *Aerospace and Electronic Systems, IEEE Transactions on*, 38(4):1344–1356.

[Goodman, 2007] Goodman, J. W. (2007). *Speckle phenomena in optics: theory and applications*. Roberts and Company Publishers.

[Graham, 1974] Graham, L. C. (1974). Synthetic interferometer radar for topographic mapping. *Proceedings of the IEEE*, 62(6):763–768.

[Guillaso and Reigber, 2005] Guillaso, S. and Reigber, A. (2005). Polarimetric SAR tomography. In *ESA Special Publication*, volume 586, page 4.

[Haas et al., 2009] Haas, C., Lobach, J., Hendricks, S., Rabenstein, L., and Pfaffling, A. (2009). Helicopter-borne measurements of sea ice thickness, using a small and lightweight, digital em system. *Journal of Applied Geophysics*, 67(3):234–241.

[Hallikainen, 1992] Hallikainen, M. (1992). Review of the microwave dielectric and extinction properties of sea ice and snow. In *Geoscience and Remote Sensing Symposium, 1992. IGARSS'92. International*, volume 2, pages 961–965. IEEE.

[Hanssen, 2001] Hanssen, R. F. (2001). *Radar interferometry: data interpretation and error analysis*, volume 2. Springer Science & Business Media.

[Hibler, 1972] Hibler, W. (1972). Removal of aircraft altitude variation from laser profiles of the arctic ice pack. *Journal of Geophysical Research*, 77(36):7190–7195.

[Hooper et al., 2004] Hooper, A., Zebker, H., Segall, P., and Kampes, B. (2004). A new method for measuring deformation on volcanoes and other natural terrains using InSAR persistent scatterers. *Geophysical research letters*, 31(23).

[Huang and Ferro-Famil, 2009] Huang, Y. and Ferro-Famil, L. (2009). 3-D characterization of buildings in a dense urban environment using L-band Pol-InSAR data with irregular baselines. In *Geoscience and Remote Sensing Symposium, 2009 IEEE International, IGARSS 2009*, volume 3, pages III–29. IEEE.

[Huang et al., 2012a] Huang, Y., Ferro-Famil, L., and Neumann, M. (2012a). Tropical forest structure estimation using polarimetric SAR tomography at P-band. In *Geoscience and Remote Sensing Symposium (IGARSS), 2012 IEEE International*, pages 7593–7596. IEEE.

[Huang et al., 2012b] Huang, Y., Ferro-Famil, L., and Reigber, A. (2012b). Under-foliage object imaging using SAR tomography and polarimetric spectral estimators. *IEEE transactions on geoscience and remote sensing*, 50(6):2213–2225.

[Krieger et al., 2007] Krieger, G., Moreira, A., Fiedler, H., Hajnsek, I., Werner, M., Younis, M., and Zink, M. (2007). TanDEM-X: A satellite formation for high-resolution SAR interferometry. *IEEE Transactions on Geoscience and Remote Sensing*, 45(11):3317–3341.

[Krieger et al., 2005] Krieger, G., Papathanassiou, K. P., and Cloude, S. R. (2005). Spaceborne polarimetric SAR interferometry: Performance analysis and mission concepts. *EURASIP Journal on Applied Signal Processing*, 2005:3272–3292.

[Kwok et al., 1992] Kwok, R., Rignot, E., Holt, B., and Onstott, R. (1992). Identification of sea ice types in spaceborne synthetic aperture radar data. *Journal of Geophysical Research: Oceans (1978–2012)*, 97(C2):2391–2402.

[Lee and Pottier, 2009] Lee, J.-S. and Pottier, E. (2009). *Polarimetric radar imaging: from basics to applications*. CRC press.

[Li and Perrie, 2016] Li, H. and Perrie, W. (2016). Sea ice characterization and classification using hybrid polarimetry SAR. *IEEE Journal of Selected Topics in Applied Earth Observations and Remote Sensing*, 9(11):4998–5010.

[Lombardini, 2005] Lombardini, F. (2005). Differential tomography: A new framework for SAR interferometry. *IEEE Transactions on Geoscience and Remote Sensing*, 43(1):37–44.

[Lombardini et al., 2003] Lombardini, F., Montanari, M., and Gini, F. (2003). Reflectivity estimation for multibaseline interferometric radar imaging of layover extended sources. *IEEE Transactions on Signal Processing*, 51(6):1508–1519.

[Lombardini and Reigber, 2003] Lombardini, F. and Reigber, A. (2003). Adaptive spectral estimation for multibaseline SAR tomography with airborne L-band data. In *Geoscience and Remote Sensing Symposium, 2003. IGARSS'03. Proceedings. 2003 IEEE International*, volume 3, pages 2014–2016. IEEE.

[Lord, 2000] Lord, R. T. (2000). *Aspects of stepped-frequency processing for low-frequency SAR systems*. PhD thesis, University of Cape Town.

[Massonnet et al., 1993] Massonnet, D., Rossi, M., Carmona, C., Adragna, F., Peltzer, G., Feigl, K., and Rabaute, T. (1993). The displacement field of the landers earthquake mapped by radar interferometry. *Nature*, 364(6433):138–142.

[Moccia and Rufino, 2001] Moccia, A. and Rufino, G. (2001). Spaceborne along-track SAR interferometry: Performance analysis and mission scenarios. *IEEE Transactions on Aerospace and Electronic systems*, 37(1):199–213.

[Moen, 2014] Moen, M.-A. N. (2014). *Analysis and Interpretation of C-band Polarimetric SAR Signatures of Sea Ice*. PhD thesis, UIT The Arctic University of Norway.

[Moreira et al., 1996] Moreira, A., Mittermayer, J., and Scheiber, R. (1996). Extended chirp scaling algorithm for air-and spaceborne SAR data processing in stripmap and ScanSAR imaging modes. *IEEE Transactions on Geoscience and Remote Sensing*, 34(5):1123–1136.

[Moreira et al., 2013] Moreira, A., Prats-Iraola, P., Younis, M., Krieger, G., Hajnsek, I., and Papathanassiou, K. P. (2013). A tutorial on synthetic aperture radar. *IEEE Geoscience and remote sensing magazine*, 1(1):6–43.

[Munson et al., 1983] Munson, D. C., O'Brien, J. D., and Jenkins, W. K. (1983). A tomographic formulation of spotlight-mode synthetic aperture radar. *Proceedings of the IEEE*, 71(8):917–925.

[Munson and Visentin, 1989] Munson, D. C. and Visentin, R. L. (1989). A signal processing view of strip-mapping synthetic aperture radar. *IEEE Transactions on Acoustics, Speech, and Signal Processing*, 37(12):2131–2147.

[Nannini et al., 2012] Nannini, M., Scheiber, R., Horn, R., and Moreira, A. (2012). First 3-D reconstructions of targets hidden beneath foliage by means of polarimetric SAR tomography. *IEEE Geoscience and Remote Sensing Letters*, 9(1):60–64.

[Nghiem, 1991] Nghiem, S. (1991). *Electromagnetic wave models for polarimetric remote sensing of geophysical media*. PhD thesis, Massachusetts Institute of Technology, Massachusetts Institute of Technology.

[NRCAN, 2015] NRCAN, N. R. C. (2015). Radar image distortions.

[NSIDC, 2017] NSIDC (2017). "Sea ice features: Introduction." National Snow and Ice Data Center. Accessed 15 July 2017.

[Oliver and Quegan, 2004] Oliver, C. and Quegan, S. (2004). *Understanding synthetic aperture radar images*. SciTech Publishing.

[Onstott and Shuchman, 2004] Onstott, R. and Shuchman, R. (2004). SAR measurements of sea ice. In Jackson, C. R., Apel, J. R., et al., editors, *Synthetic aperture radar Marin User's manual*, volume 3, pages 81–115. National Oceanic and Atmospheric Adminstration (NOAA),, Washington D.C.

[Onstott, 1992] Onstott, R. G. (1992). SAR and scatterometer signatures of sea ice. In Carsey, F. D., editor, *Microwave Remote Sensing of Sea Ice*, pages 73–104. American Geophysical Union, Washington D.C.

[Papathanassiou and Cloude, 2001] Papathanassiou, K. P. and Cloude, S. R. (2001). Single-baseline polarimetric SAR interferometry. *IEEE Transactions on Geoscience and Remote Sensing*, 39(11):2352–2363.

[Prats et al., 2009] Prats, P., Scheiber, R., Reigber, A., Andres, C., and Horn, R. (2009). Estimation of the surface velocity field of the Aletsch glacier using multibaseline airborne SAR interferometry. *IEEE Transactions on Geoscience and Remote Sensing*, 47(2):419–430.

[Rabus et al., 2003] Rabus, B., Eineder, M., Roth, A., and Bamler, R. (2003). The shuttle radar topography mission—a new class of digital elevation models acquired by spaceborne radar. *ISPRS journal of photogrammetry and remote sensing*, 57(4):241–262.

[Raney et al., 1994] Raney, R. K., Runge, H., Bamler, R., Cumming, I. G., and Wong, F. H. (1994). Precision SAR processing using chirp scaling. *IEEE Transactions on geoscience and remote sensing*, 32(4):786–799.

[Rao et al., 2004] Rao, Y., Venkataraman, G., Rao, K., et al. (2004). SAR interferometry for DEM generation and movemnet of indian glaciers. In *Geoscience and Remote Sensing Symposium, 2004. IGARSS'04. Proceedings. 2004 IEEE International*, volume 2, pages 1128–1131. IEEE.

[Reale et al., 2011] Reale, D., Fornaro, G., Pauciullo, A., Zhu, X., and Bamler, R. (2011). Tomographic imaging and monitoring of buildings with very high resolution SAR data. *Geoscience and Remote Sensing Letters, IEEE*, 8(4):661–665.

[Reigber and Moreira, 2000] Reigber, A. and Moreira, A. (2000). First demonstration of airborne SAR tomography using multibaseline L-band data. *Geoscience and Remote Sensing, IEEE Transactions on*, 38(5):2142–2152.

[Reigber et al., 2013] Reigber, A., Scheiber, R., Jager, M., Prats-Iraola, P., Hajnsek, I., Jagdhuber, T., Papathanassiou, K. P., Nannini, M., Aguilera, E., Baumgartner, S., et al. (2013). Very-high-resolution airborne synthetic aperture radar imaging: Signal processing and applications. *Proceedings of the IEEE*, 101(3):759–783.

[Rekioua et al., 2016] Rekioua, B., Davy, M., Ferro-Famil, L., and Tebaldini, S. (2016). Snowpack permittivity profile retrieval from tomographic SAR data. *sciencedirect*.

[Renner et al., 2014] Renner, A. H., Gerland, S., Haas, C., Spreen, G., Beckers, J. F., Hansen, E., Nicolaus, M., and Goodwin, H. (2014). Evidence of arctic sea ice thinning from direct observations. *Geophysical Research Letters*, 41(14):5029–5036.

[Rosen et al., 2000] Rosen, P. A., Hensley, S., Joughin, I. R., Li, F. K., Madsen, S. N., Rodriguez, E., and Goldstein, R. M. (2000). Synthetic aperture radar interferometry. *Proceedings of the IEEE*, 88(3):333–382.

[Rufino et al., 1998] Rufino, G., Moccia, A., and Esposito, S. (1998). DEM generation by means of ERS tandem data. *IEEE Transactions on Geoscience and Remote Sensing*, 36(6):1905–1912.

[Sauer et al., 2011] Sauer, S., Ferro-Famil, L., Reigber, A., and Pottier, E. (2011). Three-dimensional imaging and scattering mechanism estimation over urban scenes using dual-baseline polarimetric InSAR observations at L-band. *IEEE Transactions on Geoscience and Remote Sensing*, 49(11):4616–4629.

[Scheiber et al., 2011] Scheiber, R., De Zan, F., Prats, P., Araujo, L. S., Künemund, M., and Marotti, L. (2011). Interferometric sea ice mapping with TanDEM-X: First experiments. In *Geoscience and Remote Sensing Symposium (IGARSS), 2011 IEEE International*, pages 3594–3597. IEEE.

[Shokr and Sinha, 2015] Shokr, M. and Sinha, N. (2015). *Sea ice: physics and remote sensing*. John Wiley & Sons.

[Soh and Tsatsoulis, 1999] Soh, L.-K. and Tsatsoulis, C. (1999). Texture analysis of SAR sea ice imagery using gray level co-occurrence matrices. *IEEE Transactions on geoscience and remote sensing*, 37(2):780–795.

[Soumekh, 1999] Soumekh, M. (1999). *Synthetic aperture radar signal processing*, volume 7. New York: Wiley.

[Stiles et al., 1982] Stiles, J. A., Frost, V. S., Holtzman, J. C., and Shanmugam, K. (1982). The recognition of extended targets: SAR images for level and hilly terrain. *IEEE Transactions on Geoscience and Remote Sensing*, GE-20(2):205–211.

[Strub-Klein and Sudom, 2012] Strub-Klein, L. and Sudom, D. (2012). A comprehensive analysis of the morphology of first-year sea ice ridges. *Cold Regions Science and Technology*, 82:94–109.

[Tebaldini, 2009] Tebaldini, S. (2009). *Multi-baseline SAR imaging: Models and algorithms*. PhD thesis, POLITECNICO DI MILANO.

[Tebaldini, 2010] Tebaldini, S. (2010). Single and multipolarimetric SAR tomography of forested areas: A parametric approach. *IEEE Transactions on Geoscience and Remote Sensing*, 48(5):2375–2387.

[Tebaldini and Ferro-Famil, 2013] Tebaldini, S. and Ferro-Famil, L. (2013). High resolution three-dimensional imaging of a snowpack from ground-based SAR data acquired at X and Ku band. In *IGARSS*, pages 77–80.

[Tebaldini et al., 2016] Tebaldini, S., Nagler, T., Rott, H., and Heilig, A. (2016). Imaging the internal structure of an Alpine glacier via L-band airborne SAR tomography. *IEEE Transactions on Geoscience and Remote Sensing*, 54(12):7197–7209.

[Tebaldini and Rocca, 2012] Tebaldini, S. and Rocca, F. (2012). Multibaseline polarimetric SAR tomography of a boreal forest at P-and L-bands. *Geoscience and Remote Sensing, IEEE Transactions on*, 50(1):232–246.

[Timco and Burden, 1997] Timco, G. and Burden, R. (1997). An analysis of the shapes of sea ice ridges. *Cold regions science and technology*, 25(1):65–77.

[Tomiyasu, 1978] Tomiyasu, K. (1978). Tutorial review of synthetic-aperture radar (SAR) with applications to imaging of the ocean surface. *Proceedings of the IEEE*, 66(5):563–583.

[Ulaby and Long, 2014] Ulaby, F. and Long, D. (2014). *Microwave Radar and Radiometric Remote Sensing*. University of Michigan Press.

[Ulaby et al., 1982a] Ulaby, F. T., Kouyate, F., Fung, A. K., and Sieber, A. J. (1982a). A backscatter model for a randomly perturbed periodic surface. *Geoscience and Remote Sensing, IEEE Transactions on*, GE-20(4):518–528.

[Ulaby et al., 1982b] Ulaby, F. T., Moore, R. K., and Fung, A. K. (1982b). *Microwave Remote Sensing: Active and Passive: Radar Remote Sensing and Surface Scattering and Emission Theory*, volume 2. Addison-Wesley, Reading, MA.

[Ulander et al., 2003] Ulander, L. M., Hellsten, H., and Stenstrom, G. (2003). Synthetic-aperture radar processing using fast factorized back-projection. *Aerospace and Electronic Systems, IEEE Transactions on*, 39(3):760–776.

[Weeks and Ackley, 1986] Weeks, W. F. and Ackley, S. F. (1986). The growth, structure, and properties of sea ice. In Untersteiner, N., editor, *The geophysics of sea ice*, pages 9–164. Springer US.

[Wehner, 1987] Wehner, D. R. (1987). High resolution radar. *Norwood, MA, Artech House, Inc., 1987, 484*.

[Werner, 2001] Werner, M. (2001). Shuttle Radar Topography Mission (SRTM) mission overview. *Frequenz*, 55(3-4):75–79.

[WMO, 2014] WMO (2014). Sea ice nomenclature and international system of sea ice symbols. Technical report, World Metrereological organization, Geneva, Switzerland.

[Yitayew et al., 2017] Yitayew, T. G., Ferro-Famil, L., Eltoft, T., and Tebaldini, S. (2017). Tomographic imaging of fjord ice using a very high resolution ground-based SAR system. *IEEE Transactions on Geoscience and Remote Sensing*, 55(2):698–714.

[Zebker and Goldstein, 1986] Zebker, H. A. and Goldstein, R. M. (1986). Topographic mapping from interferometric synthetic aperture radar observations. *Journal of Geophysical Research: Solid Earth*, 91(B5):4993–4999.

[Zebker and Villasenor, 1992] Zebker, H. A. and Villasenor, J. (1992). Decorrelation in interferometric radar echoes. *IEEE Transactions on geoscience and remote sensing*, 30(5):950–959.

[Zhu and Bamler, 2009] Zhu, X. and Bamler, R. (2009). Very high resolution SAR tomography via compressive sensing. In *Proc. ESA FRINGE Workshop Adv. Sci. Appl. SAR Interferometry*.

[Zhu and Bamler, 2010a] Zhu, X. X. and Bamler, R. (2010a). Tomographic SAR inversion by $L\_\{1\}$-norm regularization—The compressive sensing approach. *IEEE Transactions on Geoscience and Remote Sensing*, 48(10):3839–3846.

[Zhu and Bamler, 2010b] Zhu, X. X. and Bamler, R. (2010b). Very high resolution spaceborne SAR tomography in urban environment. *IEEE Transactions on Geoscience and Remote Sensing*, 48(12):4296–4308.

[Zhu and Bamler, 2012] Zhu, X. X. and Bamler, R. (2012). Demonstration of super-resolution for tomographic SAR imaging in urban environment. *IEEE Transactions on Geoscience and Remote Sensing*, 50(8):3150–3157.